Fuel 408 (2026) 137642

Contents lists available at ScienceDirect

Fuel

journal homepage: www.elsevier.com/locate/fuel

Full Length Article

Low loading copper-based catalysts for effective CO_2 hydrogenation to methanol

R. González-Pizarro, S. Renda, J. Lasobras, J. Soler, M. Menéndez, J. Herguido *

Catalysis and Reactor Engineering Group (CREG) - Aragon Institute of Engineering Research (I3A), Universidad Zaragoza, c/ Mariano Esquillor s/n, 50018 Zaragoza, Spain

ARTICLE INFO

Keywords:
Methanol synthesis
Power to liquid
Copper-based catalysts
Low loading active phase catalyst
Hydrogenation of CO_2

ABSTRACT

Methanol synthesis via CO_2 hydrogenation is an emerging Power-to-Liquid (PtL) technology aimed to accelerate the energy transition and the defossilization of key sectors, particularly maritime transport. This study focuses on the study of low loading formulations, to minimize the catalyst cost. Key operational variables including temperature (*T*), Weight Hourly Space Velocity (*WHSV*), copper and zinc loadings, and aging state were systematically varied. An overall active phase loading of 10 $\%^{wt}$ emerged as optimal. Within this total loading, a 5 $\%^{wt}$Cu-5 $\%^{wt}Zn/ZrO_2$ catalysts delivered higher methanol productivity than 10 $\%^{wt}Cu/ZrO_2$; however, the bimetallic catalysts showed pronounced deactivation under water-rich atmospheres, establishing 10 $\%^{wt}Cu/ZrO_2$ as the most promising catalysts. Operating temperature and *WHSV* exerted a strong, synergistic influence on CH_3OH formation; in particular, increasing *WHSV* shifted the reaction away from thermodynamic control and boosted methanol synthesis. Finally, the catalytic performance of these low-loading catalysts was benchmarked against high-copper-loading methanol catalysts reported in the literature by critically compare their activities as a function of the residence time (τ) calculated at reaction conditions. This assessment revealed that the proposed formulation is highly competitive when compared to most conventional formulation, with a maximum methanol space time yield (STY_{CH_3OH}) of 3.9 $g_{CH_3OH}\ gCu^{-1}\ h^{-1}$. This comparison confirms that the catalysts proposed in this study could offer a remarkably more efficient use of the active phase than the conventional high-copper-loading catalysts.

1. Introduction

Global warming is among the most pressing challenges we face today [1]. Its primary driver is anthropogenic CO_2 emissions [2,3], which derives from the continuous utilization of fossil fuels [1,4,5] and has surpassed + 1 °C above preindustrial level [6,7] with concerning consequences for the increase of the global temperature [8–10]. This environmental crisis has prompted a shift away from fossil fuels toward a decentralized, or "green," energy transition [11–16]. Several alternatives are being explored: from increasing the production of renewable electricity [17] and advancing electrification [18], to adopting carbon-free fuels like NH_3 or H_2 [19–22], or even switching to synthetic fuels such as CH_4 and CH_3OH [23–27].

Among the synthetic fuels, this work focuses on a single compound: methanol [28]. This product is widely used as a raw material in industrial processes [29–36]. Additionally, it can serve as a fuel, particularly in maritime applications [37–41]. Among synthetic fuels, methanol stands out because it remains in the liquid phase under atmospheric conditions, thereby reducing both transportation and storage costs [42–44]. Green methanol synthesis by CO_2 hydrogenation is a Power-to-Liquid (*PtL*) process [38,45,46], which produces a synthetic fuel, or e-fuel (to highlight its production from green-H_2), whose combustion emits no net CO_2, thereby closing the carbon cycle [47–49].

$$CO + 2H_2 \rightleftharpoons CH_3OH \qquad \Delta H_r^0 = -90.37\ \left[kJ{\cdot}mol^{-1}\right] \tag{r.1}$$

$$CO_2 + H_2 \rightleftharpoons CO + H_2O \qquad \Delta H_r^0 = -41.21\ \left[kJ{\cdot}mol^{-1}\right] \tag{r.2}$$

$$CO_2 + 3H_2 \rightleftharpoons CH_3OH + H_2O \qquad \Delta H_r^0 = -49.16\ \left[kJ{\cdot}mol^{-1}\right] \tag{r.3}$$

The *PtL* process is highly sensitive to operating conditions from a thermodynamic standpoint [50–53]. Since methanol synthesis is an exothermic reaction (r.1 and r.3), increasing the operating temperature further limits the process thermodynamically. On the other hand, conducting the process at lower temperature faces the kinetics limitations. In addition, the operating pressure has the greatest influence, as the

* Corresponding author.
E-mail address: jhergui@unizar.es (J. Herguido).

https://doi.org/10.1016/j.fuel.2025.137642
Received 15 October 2025; Received in revised form 14 November 2025; Accepted 19 November 2025
Available online 26 November 2025

Nomenclature

$k_{0,1} - k_{0,3}$	Pre-exponential factor of reaction r.1 and r.3, mol g^{-1} s^{-1} bar^{-1}
$k_{0,2}$	Pre-exponential factor of reaction r.2, mol g^{-1} s^{-1} $bar^{-1/2}$
$E_{a,i}$	Activation energy of reaction r.i, kJ mol^{-1}
k_1, k_3	Kinetic constant of reaction r.1 and r.3, mol g^{-1} s^{-1} bar^{-1}
k_2	Kinetic constant of reaction r.2, mol g^{-1} s^{-1} $bar^{-1/2}$
K_{p1}	Equilibrium constant of reaction r.1, bar^{-2}
K_{p2}	Equilibrium constant of reaction r.2, –
K_{p3}	Equilibrium constant of reaction r.3, bar^{-3}
K_i	Adsorption constant of the *i*-species, bar
φ_i	Fugacity of the *i*-species, bar

reaction is promoted by high pressures [54].

Methanol synthesis has traditionally been conducted using copper-based catalyst, commonly combined with zinc and aluminum to form a Copper-Zinc-Alumina (CZA) catalyst via coprecipitation method [55–57]. This formulation suffers from two drawbacks. The first, although less critical, is its high concentration of transitions metals (Cu and Zn), since in many formulations aluminum accounts for only about 10–20 $\%^{wt}$ of the catalyst [58,59], which makes the catalyst expensive. The second, more significant issue, is hydrothermal deactivation, which is strictly related to the modern approach to methanol synthesis. Indeed, it conventionally relied on the use of syngas ($CO + H_2$) derived from natural gas steam reforming as feedstock [60]. However, in the pursuit of carbon–neutral fuels, methanol production is now aimed to be conducted via CO_2 hydrogenation [61]: the switch to CO_2 feedstocks leads to water formation through reactions r.2 and r.3, inducing hydrothermal deactivation of the catalyst [62–66].

Low-loading catalysts offer economic benefits and have the potentiality of presenting functional advantages as well: by reducing the amount of active metal, they lower material costs; on the other hand, the increased dispersion of the active phase can mitigate metal sintering and hydrothermal deactivation, ultimately enhancing catalyst stability and prolonging its operational lifetime. Copper is a commonly used active phase in a wide range of catalytic processes [67], but to the best of our knowledge, there are no studies in the literature focusing on the optimization of low-loading catalysts for methanol synthesis, a gap that is worth filling in light of the promises of this kind of formulation.

The present study aims to synthesize and systematically evaluate the activity and stability of low-loading copper–zinc catalysts, with the goal of identifying the optimal formulation, in terms of methanol yield. To this end, an initial screening of different catalyst compositions was performed under fixed reaction conditions, allowing for a preliminary assessment of performance. The formulation exhibiting the highest activity and stability was subsequently subjected to a more comprehensive investigation, including variation of operating conditions and stability testing, in order to fully characterize its potential in terms of CH_3OH space–time yield (STY_{CH_3OH}) and determine the factors governing its performance.

2. Materials and methods

2.1. Catalysts preparation

This study utilizes copper-based catalysts supported on zirconium oxide (ZrO_2), using a relatively low copper loading as the active phase. ZrO_2 exhibits good synergy in methanol synthesis, as this support shows high resistance under steam-rich conditions and strong affinity for CO_2 activation and adsorption. Moreover, ZrO_2 lacks intrinsic acidity, which prevents methanol from dehydrating into dimethyl ether (CH_3OCH_3). In addition, the purpose of our group is optimizing a catalytic formulation for its subsequent employment in a sorption-enhanced process to be carried out in a patented application, the continuous sorbent flux fluidized bed reaction (CSF-FBR) [68]. To this aim, many preliminary evaluations are needed, such as the optimization of the formulation, which is the core of this study. The choice of ZrO_2 as the support, in this sense, is also driven by its high mechanical strength, which is a critical requirement for operation in a fluidized bed reactor. The primary objective of this work is to determine the optimal copper content, given that traditional formulations often include around 50 $^{wt}\%$ copper [69]. In contrast, this study seeks to substantially reduce the amount of copper present in the catalyst.

A total of seven copper-based catalysts were synthesized. Five of them contained only copper, with nominal Cu loadings ranging from 5 to 15 $\%^{wt}$ in increments of 2.5 $\%^{wt}$. Two catalysts were synthetized by co-impregnating copper and zinc, maintaining a fixed total metal loading of 10 $\%^{wt}$. For these bimetallic catalysts, Cu/Zn weight ratios of 1:1 and 3:1 were employed.

Monoclinic ZrO_2, supplied by ThermoScientific, was used as the support in the preparation of all catalysts by the wet-impregnation (*WI*) method. The required amounts of copper ($Cu(NO_3)\cdot 3H_2O$, ALDO, >99 %) and zinc ($Zn(NO_3)\cdot 6H_2O$, ALDO, >98 %) precursors were dissolved in 300 mL of distilled water, and the support was added in a single impregnation step. The suspension was stirred at 150 rpm for 7 h. Residual solvent was removed at 70 °C under vacuum in a rotary evaporator (*Buchi*).

The resulting solid was calcined in two stages: (**i**) 90 °C for 4 h to ensure complete removal of physisorbed water and (**ii**) 350 °C for 3 h. Both stages were reached using a heating ramp of 2 °C min^{-1}. Finally, the calcined catalyst was sieved to 250 – 400 μm particle size range.

2.2. Experimental setup

The catalytic tests were carried out at laboratory scale using a stainless steel fixed-bed reactor 12 mm i.d., followed by a cryogenic trap submerged in an ice/salt/ethanol bath (−15 °C). A back-pressure controller was installed downstream of the liquid trap. Temperature monitoring was achieved using a K-type thermocouple positioned at the midpoint of the catalytic bed. The reactor outlet stream, consisting of both unconverted reactants and products, passed through the cryogenic trap/condenser to collect condensable compounds (H_2O and CH_3OH). Non-condensable gases were decompressed and analyzed online using an Agilent 490 MicroGC. At the conclusion of each catalytic test, the system was depressurized, and the condenser was removed to recover the accumulated liquid, which was subsequently analyzed using a Shimadzu QP2010 Ultra Gas Chromatography-Mass Spectrometry (GC–MS) system.

For all the experimental tests, the catalytic bed was diluted with inert material (quartz sand, 75 – 150 μm particle size) until a fixed volume (25.5 cm^3).

2.2.1. Catalytic tests

Prior to the catalytic tests, the catalyst required an activation stage. This procedure involved a flow of 150 mL_{STP}/min of 50/50 $\%^{v}$ H_2/Ar at 1 atmosphere for 60 min.

Once the catalyst activation stage was over, the catalytic test was immediately carried out. The system was pressurized with argon to 20 atm, once the desired operating conditions (*P* and *T*) were reached, the reaction gas mixture ($H_2 + CO_2$) was introduced. The reactor already loaded the catalyst and was filled with quartz particles to achieve the fixed volume (25.5 cm^3).

Furthermore, complementary high-pressure experiments were conducted at MOEVE (a global, integrated energy and chemicals company, formerly Cepsa). These tests were performed at their Centre for Innovation in Energy Transition (CITE, located in Madrid, Spain) using

elevated pressure, increased catalyst loadings, and higher gas flow rates (denoted by an asterisk in Table 1). These conditions resulted in correspondingly higher weight hourly space velocity (*WHSV*) values. The inert/catalyst mass ratio (*I/C*) was approximately 98 %, ensuring that the bed remained isothermal and thermally homogeneous.

The fixed and variable operating conditions are detailed in Table 1.

It should be noted that this experimental procedure introduced a significant dead volume due to argon accumulation during the pressurization of the experimental setup. At the beginning of the experiment, the interior of the reactor and condenser is occupied by Ar, which is necessary to reach the desired pressure. Consequently, when the reaction feed ($CO_2 + H_2$) is introduced, it initially remains inside the system, displacing the pre-existing Ar. This results in a dead volume (V_D) and a time lag between the feed introduction and the outlet response of the system. Therefore, to enable continuous time-resolved analysis, a blank experiment is required to characterize the system response. This blank test was conducted under the same operating conditions as the main experiments but in the absence of the catalyst, allowing the evaluation of the intrinsic system response to the step feed input.

2.2.2. Aging tests

A key performance parameter for these catalysts is their hydrothermal stability because copper-based catalysts are highly susceptible to deactivation in streams with high water–vapor partial pressure [62–64,66,70–72], which appears to be produced by hydrothermal sintering of Cu crystallites. To probe this, the catalyst was deliberately exposed to severe stream conditions: it was held at 250 °C for 75 h in a fully water-saturated gas flow to accelerate hydrothermal deactivation. This aging procedure was carried out using a quartz fixed-bed reactor with a constant water atmosphere generated by evaporating distilled water in a tank directly connected to the reactor. The aging test was carried out by evaporating 500 mL of liquid-phase H_2O as feed. The water was progressively evaporated over 75 h in a continuous N_2 stream. This amount corresponds to a water vapor flow rate of 8.2 L h^{-1} fed into the reactor containing the catalyst.

After this aging treatment, a standard catalytic activity test was performed to assess how the steam exposure affected the catalyst's efficiency.

2.3. Data treatment

Once the system response was determined through initial blank experiments, key parameters such as CO_2 conversion (Eq. (1), selectivities (Eq. (2), and yields (Eq. (3) can be analyzed. These metrics facilitate the assessment of the effects of operating temperature and Weight Hourly Space Velocity (*WHSV*).

$$CO_2\ conversion\ (\%) = x_{CO_2}\ (\%) = 100.\left(\frac{\sum n_k^{Out}\cdot s_k}{n_{CO_2}^{In}}\right) \quad (1)$$

Table 1
Fixed and variable operating conditions.

Parameter	Value
Solids volume, V_s (cm^3)	25.5
H_2: CO_2 molar ratio	3
Pressure (atm)	20 – 30* – 40*
Time on stream, *TOS* (min)	130
Catalyst load, W_{cat} (g)	0.5 – 0.6 – 0.75 – 1 – 4*
WHSV ($L_{STP}\ g_{cat}^{-1} h^{-1}$)	6 – 8 – 10 – 12* – 18* – 24*
Temperature, *T* (°C)	220 – 240—260
Flow rate q_0 ($mL_{STP}\ min^{-1}$)	100 – 800* – 1200* – 1600*
Catalyst (–)	M%^{wt}Cu/ZrO_2 (M = 5; 7.5; 10; 12.5; 15) M%^{wt}Cu-N%^{wt}Zn/ZrO_2 (i) M = 5.0 and N = 5.0 (ii) M = 7.5 and N = 2.5

* carried out at the CITE (MOEVE) facilities.

$$k\ selectivity\ (\%) = S_k\ (\%) = 100.\left(\frac{s_k\cdot n_k^{Out}}{\sum n_k^{Out}\cdot s_k}\right) \quad (2)$$

$$k\ yield\ (\%) = \eta_k\ (\%) = \frac{x_{CO_2}.S_k}{100}(\%) = 100.\left(\frac{s_k\cdot n_k^{Out}}{n_{CO_2}^{In}}\right) \quad (3)$$

$$STY_{CH_3OH}\left(mg_{CH_3OH}g_{Cu}^{-1}h^{-1}\right) = STY_{CH_3OH} = \frac{n_{CO_2}^{In}\cdot(\eta_{kCH_3OH}/100)\cdot M_{w,CH_3OH}}{W_{Cu}\cdot(TOS/60)} \quad (4)$$

k = product (CO and CH_3OH)
s = stoichiometric coefficient ($s = 1$ for CO and CH_3OH)
$M_{w,k}$ = molecular weight of the product k (mg/mmol)

In these equations, n_k^{Out} and n_k^{In} represent the cumulative molar amounts (mmol) of each compound exiting and entering the reactor, respectively, over the entire experiment. The moles of gaseous products and unconverted reactants leaving the system were determined by integrating the exiting molar flow rates (F_k^{Out})monitored via μGC over time during the experiment (Eq. (5). The total moles of condensable products were quantified by weighing and analyzing the liquid fraction using GC–MS. Additionally, material closure balances were performed for each element present in the system (C, H, and O) to ensure consistency in mass accounting. In all experiments the atomic mass balance error was smaller than 2 %.

$$n_k^{Out} = \int_{t=0}^{t=end} F_k^{Out}\cdot dt \quad (5)$$

The conventional descriptors Gas/Weight Hourly Space Velocity (*GHSV/WHSV*) suffer from an inherent limitation: they depend on the operating temperature (*T*) and pressure (*P*) because the volumetric flow rate of a gas changes with both variables. Thus, keeping the same *GHSV* or *WHSV* while altering *T* or *P* inevitably shortens or lengthens the actual residence time in the rector. To avoid this ambiguity, the present work analyses catalytic performance in terms of effective residence time, τ, considered as the space time under the operating conditions in the catalytic bed (T_{Op} and P_{Op}); that is, the time required for the feed gas to traverse the catalyst bed. τ is calculated from the inlet volumetric flow rate at the experimental temperature (T_{Op}) and pressure (P_{Op}), ensuring that experiments are compared under truly identical operating conditions (Eq.6).

$$\tau(s) = \frac{P_{Op}\cdot T_{STP}\cdot 3600}{P_{STP}\cdot T_{Op}\cdot GHSV} \quad (6)$$

2.4. Kinetic model

For evaluating the kinetic behavior of the catalysts employed in the present study, the model proposed by Graaf *et al.* [73] and recently recalculated by van Kampen *et al.* [74] was employed. It is a three-reactions model: methanol is potentially produced from CO_2 (r.3) and from CO (r.1) with a stepwise mechanism, where *rWGS* reaction (r.2) offers the first reaction step and describes the conversion of CO_2 into CO. The equilibrium constants K_p (with $p = 1, 2, 3$) and the adsorption constants K_i (with i = CO, CO_2, H_2O and H_2) were retrieved from [74]. The kinetic analysis is based on the hypotheses of: ideal conditions, isothermal reactor, plug flow, and absence of mass transfer limitations. Kinetic constants were calculated based on the Arrhenius equation (Eq.16) where k_i is the kinetic constant of the i reaction, and $E_{a,i}$ and $k_{0,i}$ represent its activation energy and pre-exponential factor. All the equations and parameters are listed in Table 2.

The Euler method was used for the discretization of the system and the optimization of the parameters was based on the minimization of an objective function defined as eq. (17), where *c* represents the

Table 2
Rate equations and parameters of the applied kinetic model.

$r_1 = \frac{k_3 K_{CO}\left[\varphi_{CO}\varphi_{H2}^{3/2} - \varphi_{CH3OH}/\left(\varphi_{H2}^{1/2}K_{p1}\right)\right]}{(1+K_{CO}\varphi_{CO}+K_{CO2}\varphi_{CO2})\left[\varphi_{H2}^{1/2}+\left(K_{H2O}/K_{H2}^{1/2}\right)\varphi_{H2O}\right]}$	Eq. (7)
$r_2 = \frac{k_2 K_{CO2}\left[\varphi_{CO2}\varphi_{H2} - \varphi_{CO}\varphi_{H2O}/K_{p2}\right]}{(1+K_{CO}\varphi_{CO}+K_{CO2}\varphi_{CO2})\left[\varphi_{H2}^{1/2}+\left(K_{H2O}/K_{H2}^{1/2}\right)\varphi_{H2O}\right]}$	Eq. (8)
$r_3 = \frac{k_1 K_{CO2}\left[\varphi_{CO2}\varphi_{H2}^{3/2} - \varphi_{CH3OH}\varphi_{H2O}/\left(\varphi_{H2}^{3/2}K_{p3}\right)\right]}{(1+K_{CO}\varphi_{CO}+K_{CO2}\varphi_{CO2})\left[\varphi_{H2}^{1/2}+\left(K_{H2O}/K_{H2}^{1/2}\right)\varphi_{H2O}\right]}$	Eq. (9)
$K_{CO} = 7.99x10^{-7} exp\left(\frac{58100}{RT}\right)$	Eq. (10)
$K_{CO2} = 1.02x10^{-7} exp\left(\frac{67400}{RT}\right)$	Eq. (11)
$K_{H2O}/K_{H2}^{\frac{1}{2}} = 4.13x10^{-11} exp\left(\frac{104500}{RT}\right)$	Eq. (12)
$log_{10}K_{p1} = \frac{5139}{T} - 12.621$	Eq. (13)
$log_{10}K_{p2} = \frac{-2073}{T} + 2.029$	Eq. (14)
$K_{p3} = K_{p1}xK_{p2}$	Eq. (15)
$k_i = k_{0,i}\exp(-E_{a,i}/RT)$	Eq. (16)

experimental condition (in the present case the temperature, varying in the three conditions 220, 240 and 260 °C), $X_{exp,c}$ represents the experimental value of test c and $X_{mod,c}$ represents the model results for the c condition.

$$f = \min\left(\sum_{c=1}^{n}\left(X_{exp_c} - X_{mod_c}\right)^2\right) \quad (17)$$

3. Results and Discussion

3.1. Characterization

Characterization encompassed specific surface area (SSA), X-ray fluorescence (XRF) and X-ray diffraction (XRD). SSA was determined in a Quantachrome Autosorb iQ3 sorptometer, with values calculated from N_2-adsorption isotherms using the Brunauer-Emmet-Teller (BET) equation. Elemental composition was measured by XRF on a Thermo Fisher Scientific PERFORM-series spectrometer fitted with a Rh anode; semi-quantitative, pattern-less evaluation (sequential F → U) was performed with UNIQUANT software. XRD patterns were collected on a Rigaku RU-2500 diffractometer equipped with a rotating Cu anode (40 kV, 80 mA) and graphite monochromator to isolate Cu Kα radiation; data were recorded over $5° \leq 2\theta \leq 70°$ with a 0.03° step. Hydrogen temperature-programmed reduction (H_2-TPR) measurements were carried out on a Quantachrome iQ3 chemisorption analyzer operated with TPR-Win software. Approximately 0.2 g of the catalyst was loaded into a quartz U-tube reactor and subjected to a three-step sequence: (**i**) degassing, performed at 140 °C with a heating rate of $\beta_1 = 20$ °C min^{-1} for 30 min under flowing N_2; (**ii**) cooling to a room temperature while maintaining the inert purge; and (**iii**) TPR analysis, conducted with a 5 %^{v} H_2/N_2 mixture using a heating rate of $\beta_2 = 5$ °C min^{-1} up to 500 °C. Hydrogen consumption was monitored online with a thermal-conductivity detector (TCD).

The surface elemental composition of the catalyst particles was analyzed by Energy-Dispersive X-ray Spectroscopy (EDX) using an Inspect F-50 SEM instrument, as illustrated in Fig. 3. The images reveal a homogeneous distribution of Cu (green) active sites and Zr (red) support over the catalyst surface. Furthermore, the quantitative elemental results obtained from EDX (not shown) are consistent with the elemental composition determined by XRF analysis (Table 4).

3.1.1. H_2-TPR analysis

Fig. 1 presents the H_2-TPR profiles of all calcined catalysts: five monometallic Cu/ZrO_2 samples with different copper weight loadings and two Cu-Zn bimetallic formulations. The colored solid lines correspond to the overall reduction signal, whereas the deconvolution of individual peaks is represented as overlapping colored areas of different intensities. As the Cu loading was increased, the first maximum (associated with highly dispersed CuO species or very small crystallites) shifted from 150 °C to 180 °C, while the peak assigned to less dispersed CuO larger crystallites (centered at 200 °C) became more intense. For the bimetallic catalysts, incorporation of zinc markedly lowered the intensity of the first peak and shifted both reduction maxima to higher temperatures, evidencing a strong Cu-Zn interaction.

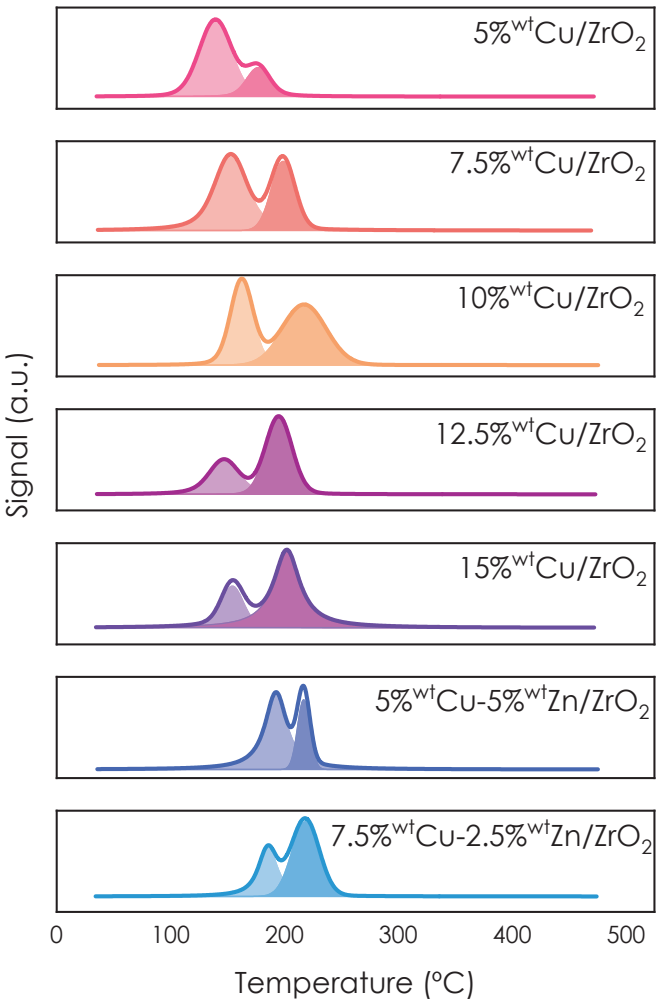

Fig. 1. H_2-TPR profiles of calcined catalysts.

The H_2-TPR profiles of the seven catalysts exhibited two reduction peaks. The first peak gradually decreased as the active-phase loading, particularly copper, increased. Table 3 presents the percentage contribution of each peak to the total hydrogen consumption.

Table 3
Percentage contribution of each reduction peak to the total H_2 consumption for the studied catalysts.

Catalyst	H_2 uptake (%)	
	First peak	Second peak
5 %^{wt}Cu/ZrO_2	75.4	24.6
7.5 %^{wt}Cu/ZrO_2	57.8	42.2
10 %^{wt}Cu/ZrO_2	53.4	46.6
12.5 %^{wt}Cu/ZrO_2	27.9	72.1
15 %^{wt}Cu/ZrO_2	26.5	73.5
5 %^{wt}Cu-5 %^{wt}Zn/ZrO_2	66.0	34.0
7.5 %^{wt}Cu2.5 %^{wt}Zn/ZrO_2	34.5	65.5

The H_2 uptake of each peak showed a strong dependence on the active-phase loading on the support surface, particularly on the copper content in the bimetallic catalysts. The first peak (associated with the reduction of the surface, homogeneous, and highly dispersed active phase) decreased in intensity as the copper loading increased. In contrast, the second peak (related to agglomerated and less dispersed active species) displayed the opposite behavior. As the copper content increased, the catalyst evolved from a highly dispersed to a selectively agglomerated state, as also observed in the FESEM/EDX images (Fig. 2), leading to an increase in the intensity of the second peak. Regarding the bimetallic catalysts, although the total active-phase loading was fixed at 10 %^{wt}, a clear trend reflecting the Cu–Zn interaction was observed. Zinc exhibited higher reducibility; at higher Zn contents, the first peak showed greater intensity, while decreasing the Zn amount on the catalyst surface led to an increase in the contribution of the second peak, corresponding to larger crystallite sizes.

3.1.2. XRF and BET

Table 4 presents the results of BET and XRF analyses for the calcined catalysts and some aged samples.

Upon impregnation with copper or copper-zinc, the catalysts exhibited a progressive reduction in specific surface area (S_{BET}) as the nominal metals loading was increased. In contrast, the samples subjected to the aging test preserve their original surface area, consistent with the fact that the combined metals accounted for only 10 %^{wt} of the overall solid, thus limiting pore blockage and sintering during thermal exposure.

The average pore size remained unchanged, both with varying active-phase loadings on the support surface and after subjecting the catalyst to the aging test; as well, the same average value was found for the spent catalysts. This can be attributed to the generally low amount of active phases, that makes the pore size distribution basically determined by the support. As well, no relevant changes in the specific surface area of the fresh catalysts were noticed after use, showing a reduction of about 3 % for all samples. In contrast, the catalysts that underwent a prior aging exhibited a more pronounced decrease in surface area after reaction, with a reduction of approximately 22 %. This loss was attributed to the sintering and agglomeration of copper and zinc particles, and indicated that the aging procedure affected the samples, inducing higher mobility of the active phases, with sintering only occurring during reaction.

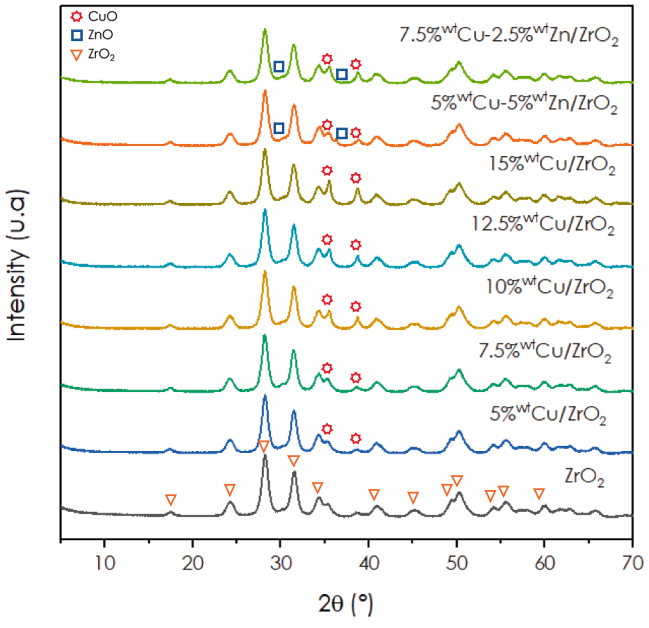

Fig. 2. XRD patterns of calcined catalysts: (**a**) ZrO_2; (**b**) 5%^{wt}Cu/ZrO_2; (**c**) 7.5%^{wt}Cu/ZrO_2; (**d**) 10%^{wt}Cu/ZrO_2; (**e**) 12.5%^{wt}Cu/ZrO_2; (**f**) 15%^{wt}Cu/ZrO_2; (**g**) 7.5%^{wt}Cu-2.5%^{wt}Zn/ZrO_2; (**h**) 5%^{wt}Cu-5%^{wt}Zn/ZrO_2.

Table 4
Catalysts specifications (XRF and BET results).

Catalyst	Cu (%^{wt})	Zn (%^{wt})	S_{BET} fresh (m^2/g)	S_{BET} spent (m^2/g)	Average pore radius (Å)
5 %^{wt}Cu/ZrO_2	5.02	–	89.0 ± 0.2	86.5	36.5
7.5 %^{wt}Cu/ZrO_2	7.47	–	88.2 ± 0.2	86.3	36.3
10 %^{wt}Cu/ZrO_2	9.93	–	87.2 ± 0.2	84.5	36.1
12.5 %^{wt}Cu/ZrO_2	12.56	–	85.6 ± 0.2	82.1	36.5
15 %^{wt}Cu/ZrO_2	14.89	–	81.3 ± 0.2	79.0	36.2
5 %^{wt}Cu-5 %^{wt}Zn/ZrO_2	5.05	5.10	88.7 ± 0.2	87.0	36.2
7.5 %^{wt}Cu-2.5 %^{wt}Zn /ZrO_2	7.43	2.53	89.1 ± 0.2	82.7	36.2
10 %^{wt}Cu/ZrO_2 (aged)	9.92	–	87.3 ± 0.2	70.3	36.3
5 %^{wt}Cu-5 %^{wt}Zn/ZrO_2 (aged)	5.03	5.09	86.3 ± 0.2	71.6	36.6

3.1.3. XRD spectra

Fig. 2 shows the X-ray diffractions patterns of all calcined catalysts; the monoclinic ZrO_2 support is included for visual reference.

The discrimination of minor oxides phases within the diffraction patterns is inherently challenging because the dense array of reflections arising from monoclinic ZrO_2 masked many secondary signals (Fig. 2), while the low nominal loadings of Cu and Zn further diminish the peak intensities of their corresponding oxides. Fig. 2 shows the XRD pattern of m-ZrO_2, confirming that the support used corresponds to the monoclinic phase. The diffractogram reveals high crystallinity and the absence of peaks associated with tetragonal or cubic phases. Seven characteristic diffraction peaks were identified at 2θ values of 24° (011), 28.2° (−111), 31.5° (111), 34.3° (200), 35.3° (002), 50.3° (022), and 60.1° (220).

Nevertheless, tenorite-type CuO can be unequivocally recognized in every catalyst, its intensity was enhanced with the increase in nominal loading of Cu, with the reflections at 35.5° (111) and 38,7° (200) (JCPDS card 45–0937). In the bimetallic formulations, wurtzite-type ZnO was likewise detected via its characteristic peaks at 31.8° and 36.3°, corresponding to the (100) and (101) planes listed in (JCPDS card 36–1451).

3.1.4. FESEM/EDX

Fig. 3 presents the FESEM/EDX analysis of the support (ZrO_2) and three copper-based catalysts containing 5, 10, and 15 %^{wt} of Cu, corresponding to the lowest, a medium, and the highest copper loadings, respectively, in order to evaluate the copper dispersion.

In the first column (FESEM), the surface morphology of both the support and the catalysts was presented. The pure zirconia sample exhibited a relatively uniform texture, composed of fine and well-dispersed nanoparticles with a rough surface typical of high surface area oxide support. Upon copper incorporation, subtle morphological variations were observed. For the catalyst containing 5 %^{wt} Cu, the particles remained small and evenly distributed over the support, with no clear evidence of metallic segregation. In the case of the 10 %^{wt} Cu/ZrO_2 catalyst, some larger aggregates started to appear, and the surface became slightly less homogeneous, suggesting the partial coalescence of metallic domains. Finally, the 15 %^{wt} Cu/ZrO_2 sample displayed a distinctly more heterogeneous structure, characterized by larger particles and clear Cu agglomerations, indicating a reduced metal dispersion at higher copper loadings.

The EDX analysis corroborated these morphological observations by

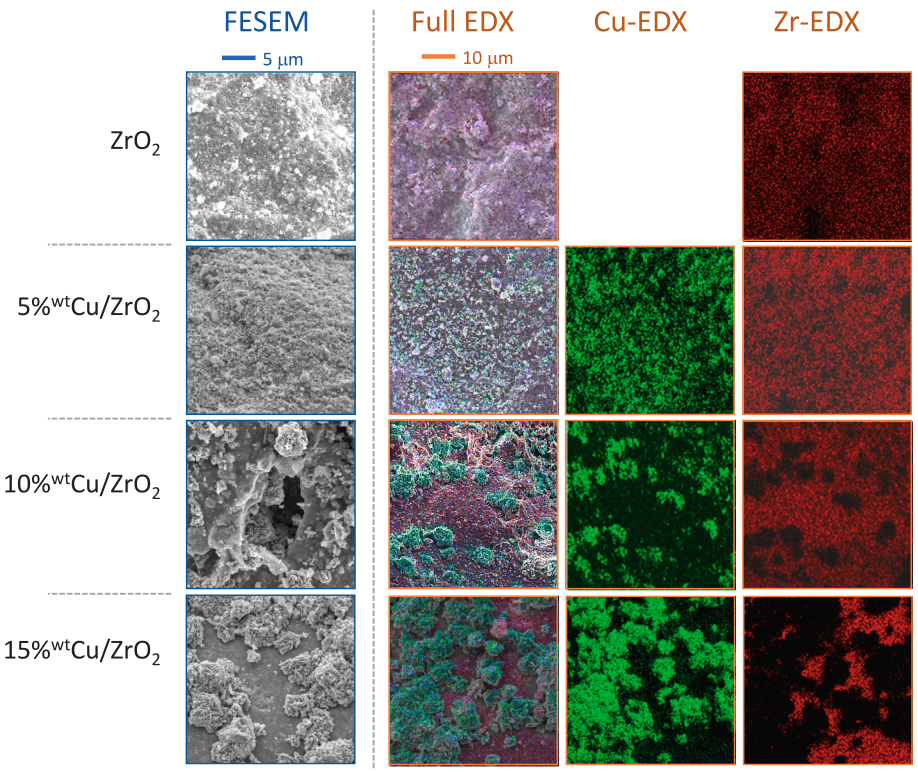

Fig. 3. FESEM and EDX analysis for the support (ZrO_2) and 5, 10 and 15 wt% of Cu over ZrO_2 showing the dispersion of the copper.

providing detailed information on the elemental composition and spatial distribution of copper across the catalyst surface. The full EDX maps showed the combined presence of Zr, and Cu, illustrating how their distribution changed with increasing copper content. For the bare ZrO_2, only the zirconium signal (red) was detected, uniformly distributed throughout the surface, confirming the compositional homogeneity of the support and the absence of metallic impurities. In the catalyst with 5 $\%^{wt}$ Cu/ZrO_2, the Cu map (green) revealed a finely dispersed and homogeneous distribution of the metal over the entire surface. The continuous Zr signal suggested that Cu was well dispersed in the form of small particles or highly divided species, likely anchored to the surface sites of ZrO_2. This type of distribution was typically associated with strong metal–support interactions, which could enhance the thermal stability and accessibility of active sites during the catalytic reaction.

When the copper loading increased to 10 $\%^{wt}$, a clear evolution in the dispersion pattern was detected. The Cu-EDX map showed regions with higher signal intensity, indicating the formation of Cu-enriched zones. Although the overall distribution was still relatively uniform, the appearance of these brighter areas evidenced the onset of agglomeration, where Cu particles began to coalesce partially. This phenomenon was likely related to the saturation of available anchoring sites on the ZrO_2 surface, leading to a decrease in the effective metal dispersion.

At the highest loading, 15 $\%^{wt}$ Cu, the elemental mapping revealed a clear segregation between the Zr and Cu signals. The copper distribution became markedly heterogeneous, with large, high-intensity regions corresponding to metallic or oxidized Cu aggregates. These agglomerates reduced the active surface area of the metal phase, which could negatively influence both the activity and selectivity of the catalyst. Overall, the EDX results confirmed that low copper loadings (around 5 $\%^{wt}$) led to a more uniform and finely dispersed catalyst, whereas increasing the metal content promoted particle growth and the formation of larger metallic domains.

The copper particle size on the catalyst surface shown a strong dependence on the total copper loading, as higher Cu content led to a clear trend toward agglomeration and heterogeneous distribution. The catalyst with the lowest Cu loading, 5 $\%^{wt}$ Cu/ZrO_2, exhibited an average particle size of approximately 3 μm, with high dispersion and homogeneity. As the Cu loading increased, these particles gradually agglomerated, resulting in an average size of around 8 μm and reduced copper dispersion. When the copper content on the catalyst surface was tripled (15 $\%^{wt}$), the particles further agglomerated into irregularly shaped copper clusters with an average size of about 15 ± 5 μm, yielding a highly heterogeneous surface morphology.

3.2. Copper loading

Fig. 4 illustrates how the copper mass fraction in the catalyst influenced (**a**) CO_2 conversion and (**b**) CH_3OH yield.

The copper mass fraction in the catalyst ($\%^{wt}$Cu) had a pronounced impact on both CO_2 conversion and CH_3OH yield (Fig. 4). Raising the reaction temperature increased the intrinsic reaction rate [75], which manifests as a higher CO_2 conversion (Fig. 4a). CH_3OH yield, however, did not rise monotonically owing to two factors: (**i**) the increased reaction rate (r.1 and r.3) and (**ii**) the limited thermodynamic equilibrium of the exothermal process. As the temperature climbs, the equilibrium yield becomes more restrictive even though the kinetic rate is enhanced. Consequently, increasing the temperature from 240 °C to 260 °C led to a decline in CH_3OH yield because thermodynamic limitations prevailed.

Both performance metrics exhibit a clear maximum as a function of copper loading: 10 $\%^{wt}$ Cu afforded the highest CO_2 conversion and CH_3OH yield. Catalysts synthesized by wet impregnation (WI) showed a measurable decline in catalytic performance once the active phase loading exceeds 10 $\%^{wt}$. This behavior reflects the competition between two antagonistic effects. Increasing the Cu mass fraction augments the surface density of metallic Cu^0 sites, thereby enhancing the intrinsic reaction rate. Simultaneously, excess Cu suppresses the formation of vacancies-critical defect sites that mediate CO_2 adsorption and activation on ZrO_2. The constrictive contribution of additional Cu^0 sites and the detrimental impact of vacancy depletion intersected at an optimum of 10 $\%^{wt}$ Cu, which delivers the highest catalytic activity within the

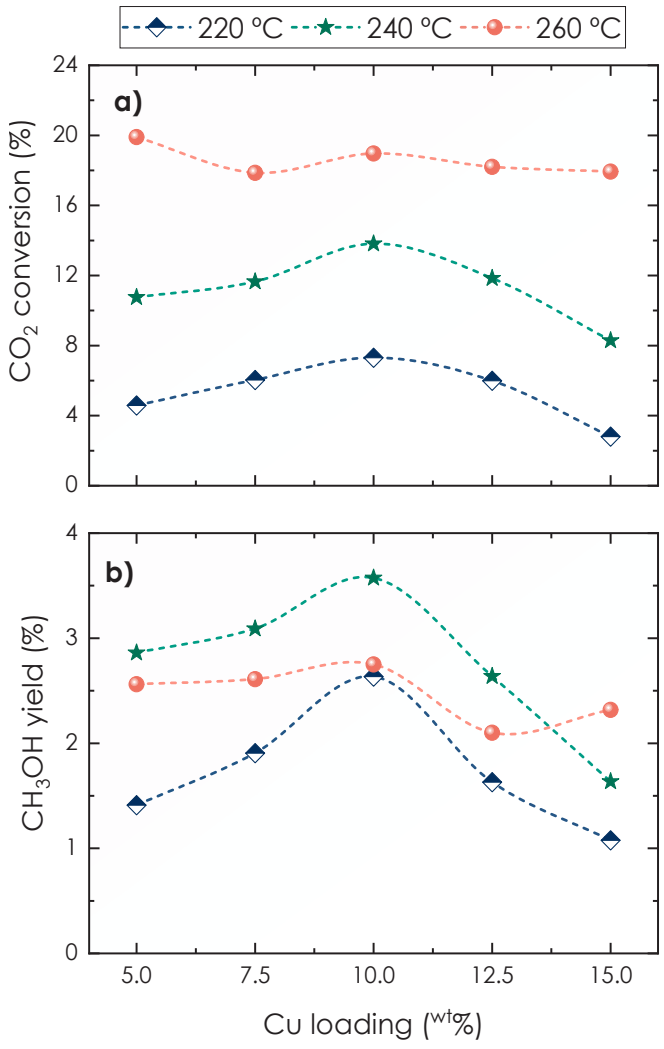

Fig. 4. CO_2 conversion (**a**) and CH_3OH yield (**b**) as a function of copper loading (^{wt}%Cu). *WHSV* = 6000 mL_{STP} $g_{cat}^{-1}h^{-1}$. Dashed lines only for visual guidance.

series investigated. This optimum is consistent with prior works by Vu *et al.* [76] and Zhou *et al.* [77], who observed analogous maxima near 8 % ^{wt}Cu.

The observed trend in catalytic activity as a function of copper loading, showing an optimum at 10 %^{wt}Cu followed by a noticeable decrease at 15 %^{wt}, was closely related to the dispersion of copper species and the strength of the metal–support interaction. At low copper content, particularly for the 5 %^{wt} Cu/ZrO_2 catalyst, the copper was highly dispersed and uniformly distributed over the zirconia surface. This high dispersion favored intimate contact between the copper and the ZrO_2 support, promoting strong metal–support interactions that enhanced both the activation of reactant molecules and the stability of the active sites during the reaction. As a result, this catalyst exhibited a balanced combination of surface accessibility and stability, which contributed to its good catalytic performance. As the copper loading increased to 10 %^{wt}, the catalytic activity reached its maximum. This behavior suggested that an intermediate copper concentration provided an optimal balance between the number of active sites and their dispersion. At this composition, sufficient copper species were available to form active surface ensembles without yet suffering from severe aggregation. Moreover, the interaction between Cu and the ZrO_2 support likely remained strong enough to stabilize the dispersed metallic phase, resulting in the highest overall activity. However, when the copper loading was further increased to 15 %^{wt}, a decline in catalytic activity was observed. This reduction was attributed to the progressive segregation and agglomeration of copper particles, as confirmed by the FESEM and EDX analyses discussed in Fig. 3. Such agglomeration led to a decrease in the active surface area and, consequently, to fewer accessible active sites for the reaction. Additionally, the formation of larger copper clusters weakened the interfacial contact with the zirconia support, reducing the beneficial metal–support interaction that had previously stabilized the active phase.

Fig. 5 shows the dependency of CH_3OH selectivity on CO_2 conversion for catalysts with different copper loadings; dashed lines represented *iso*-yield contours.

Fig. 5 reveals a clear trend: as CO_2 conversion rises, selectivity toward CH_3OH falls. This behavior stems from three factors. (**i**) the exothermic character of the methanol-forming reactions (r.1 and r.3); (**ii**) the inherently low thermodynamic ceiling of the overall process; and (**iii**) operation near that limit. Because reactions r.1 and r.3 are exothermic and therefore thermodynamically favored only at low temperatures, increasing the reaction temperature lowers the attainable CH_3OH equilibrium yield [51–53]. Running near the thermodynamic limit means CO_2 conversion approaches its maximum feasible value, with CO becoming the majority product. Operating temperature exerts a strong effect: increasing it shifts the data so that CO_2 conversion rises while CH_3OH selectivity declines. Each cluster of points bearing the same symbol lies close together, and the dispersion in CO_2 conversion and CH_3OH selectivity induced by differences in the Cu mass fraction narrows as temperature increases. The highest-temperature experiment (T = 260 °C, spheres symbols) show this scatter to be almost eliminated, indicating that all catalysts approach thermodynamic-equilibrium performance under those conditions. Consistently, CO is the major product and every measured CH_3OH selectivity remains below 50 %.

Regarding the effect of the copper mass fraction, the catalyst containing 10 %^{wt}Cu (purple symbols) exhibits the highest methanol productivity, a result consistent with the CH_3OH yield (Fig. 4b). This formulation provided results closest to the 3–4 % *iso*-yield contour, settling its superior performance. In contrast, the samples at the compositional limits-5 %^{wt}Cu and 15 %^{wt}Cu-show roughly the lowest intrinsic catalytic activity, underscoring the non-linear dependence of activity on copper loading.

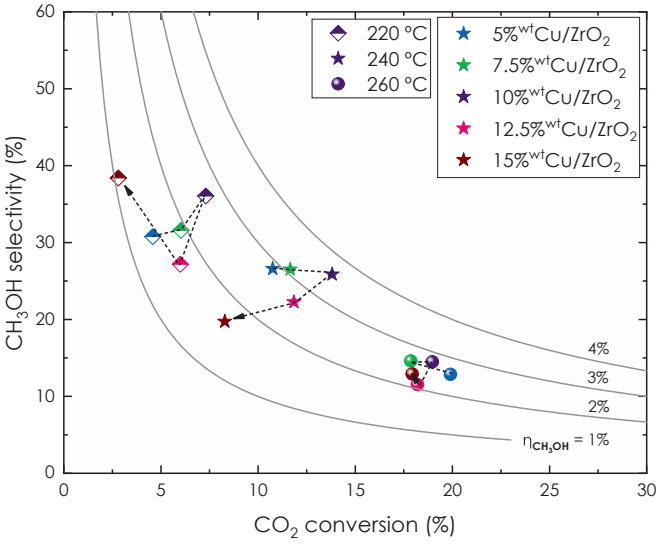

Fig. 5. CH_3OH selectivity as a function of CO_2 conversion. Catalyst and Temperature (*T*) represented with different colors and symbols, respectively. *WHSV* = 6000 mL_{STP} $g_{cat}^{-1}h^{-1}$. Dashed lines only for visual guidance (Cu content rise).

3.3. Zinc doping

Industrial methanol-synthesis catalysts, although copper-based, commonly incorporate zinc as a structural and electronic promoter [78–82]. Accordingly, fine-tuning the Cu-Zn composition of the active phase is a central optimization variable. Maintaining the total active-phase loading at the previously identified optimum of 10 %^{wt} (Figs. 4 and 5), two new formulations were prepared in which copper and zinc were present at Cu/Zn mass ratios of 1/1 and 3/1 (W_{Cu}/W_{Zn}), respectively.

Fig. 6 illustrates the influence of CO_2 conversion on the selectivity toward CH_3OH over catalysts with different copper/zinc mass fraction with a 10 % of total active phase loading; *iso*-yield lines are indicated by continuous traces.

The addition of zinc to the catalyst modified both the CO_2 conversion and the CH_3OH selectivity. At low temperatures, zinc had a detrimental effect in terms of CO_2 conversion, whereas at higher temperatures, its impact (either positive or negative) depended on the mass ratio between the two metals. Fig. 6 shows that introducing zinc at low Cu/Zn ratio led to a decrease in performance, while using an equimass ratio of zinc to copper resulted in enhanced CO_2 conversion and CH_3OH selectivity.

When a small amount of zinc was added (blue symbols), a significant decrease in CO_2 conversion was observed at all temperatures, although the CH_3OH selectivity increased. However, the product of both parameters (CH_3OH yield) remained lower than that achieved with the reference 10 %^{wt}Cu/ZrO_2 catalyst. Conversely, when zinc was added in equal mass to copper (pink symbols), a marked positive effect was observed at higher temperatures, reaching the maximum methanol yield in this study at 240 °C (pink star). Notably, this Cu/Zn mass ratio is consistent with that commonly used in the synthesis of the CuO-ZnO-Al_2O_3 catalyst, whose traditional formulation is 45/45/10, maintaining a 1:1 Cu/Zn ratio.

3.4. Aging tests

The main limitation of copper-based catalysts lies in their pronounced deactivation in the presence of moisture. Water formed as by-product during the methanol synthesis reaction is primarily responsible for this deactivation. To simulate and accelerate this phenomenon, the catalysts were exposed to an atmosphere with a high concentration of water vapor. As aforementioned, the objective of these tests was to promote rapid deactivation (i.e., to artificially age the catalyst). Subsequently, the aged catalysts were subjected to catalytic tests in order to evaluate the impact of aging on their catalytic performance.

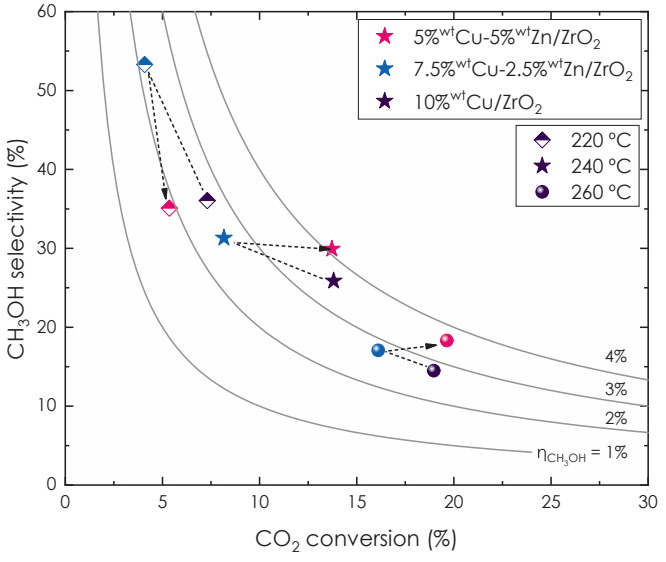

Fig. 6. CH_3OH selectivity vs CO_2 conversion for the bimetallic catalysts. Catalyst and Temperature (*T*) represented with different colors and symbols, respectively. *WHSV* = 6000 mL_{STP} $g_{cat}^{-1}h^{-1}$. Dashed lines only for visual guidance (Zn content rise).

Fig. 7 shows the catalytic activity of the most active catalysts, including both the copper-only formulation (10 %^{wt}Cu/ZrO_2) and the bimetallic formulation containing zinc (5 %^{wt}Cu-5 %^{wt}Zn/ZrO_2), in their fresh and aged states.

The aging tests revealed a significant effect on catalytic activity (Fig. 6). Both catalysts subjected to the aging process exhibited a marked decrease in catalytic performance. The extent of deactivation depended on the specific metals present in the catalyst formulation.

The catalyst containing zinc experienced a more pronounced deactivation than the catalyst composed solely of copper. This behaviour can be attributed to structural and chemical factors. Firstly, ZnO is more susceptible to sintering under the influence of water vapor. This sintering leads to significant crystal growth of ZnO, which alters its surface distribution and reduces the number of active Cu-ZnO interface sites [83,84]. In contrast, metallic copper tends to retain its crystalline structure with higher chemical and structural stability in the presence of steam [84,85].

Water vapor can also promote the hydration of ZnO, leading to the formation of amorphous species that are chemically inert under reaction conditions, potentially blocking active sites [86]. This transformation simultaneously exerts a detrimental effect by waking the synergistic interaction between Cu and ZnO, thereby diminishing the promotional role of zinc in the catalyst [87,88].

Hydrothermal deactivation of both catalysts was more pronounced in terms of CO_2 conversion (Figs. 7a and 7b), which decreased significantly after the aging tests. Specifically, CO_2 conversion dropped to roughly 20 % for the 10 %^{wt}Cu/ZrO_2 catalyst and to over 50 % for 5 %^{wt}Cu-5 %^{wt}Zn/ZrO_2 catalyst. In contrast, CH_3OH yield showed a comparatively lower decline (Figs. 7c and 7d), with a reduction of around 10 % for the Cu-only catalyst and over 50 % for the Zn-containing catalyst. This deactivation effect also depended strongly on the reaction temperature. At lower temperatures, the impact of deactivation was more severe, whereas at higher temperatures, its effect was significantly reduced. This behaviour is attributed to the enhancement of reaction kinetics with increasing temperature, which partially offset the loss of catalytic activity.

Interestingly, despite the overall reduction in performance, the aged catalyst exhibited higher CH_3OH selectivity than their fresh counterparts. This increase in selectivity was reflected in the fact that CO_2 conversion declined more sharply than CH_3OH yield, thereby raising the proportion of CO_2 converted to CH_3OH.

3.5. WHSV and τ influence

Methanol production (expressed as S_{CH3OH} or η_{CH3OH}), exhibited a strong dependence on CO_2 conversion (X_{CO2}), as operating closer to thermodynamic equilibrium generally resulted in lower CH_3OH selectivity, a trend clearly observed in Figs. 5 and 6. Therefore, achieving high CH_3OH selectivity required operating under conditions of low CO_2 conversion [89]. Additionally, CO_2 conversion in the process was strongly influenced by the Weight Hourly Space Velocity (*WHSV*). Lower *WHSV* values led to longer residence times, which in turn favoured higher CO_2 conversion. Consequently, exploring a broader range of *WHSV* values beyond those previously employed was expected to result in increased CH_3OH production.

Fig. 8 illustrate the influence of CO_2 conversion on CH_3OH selectivity across different Weight Hourly Space Velocity (*WHSV*). The 10 %^{wt}Cu/ZrO_2 catalyst was selected over the 5 %^{wt}Cu-5 %^{wt}Zn/ZrO_2 catalyst because the latter exhibited significant deactivation after the aging test (Fig. 7), resulting in a shorter operational lifetime.

Fig. 8 clearly shows a strong inverse relationship between CO_2 conversion and CH_3OH selectivity at any operating temperature. As CO_2

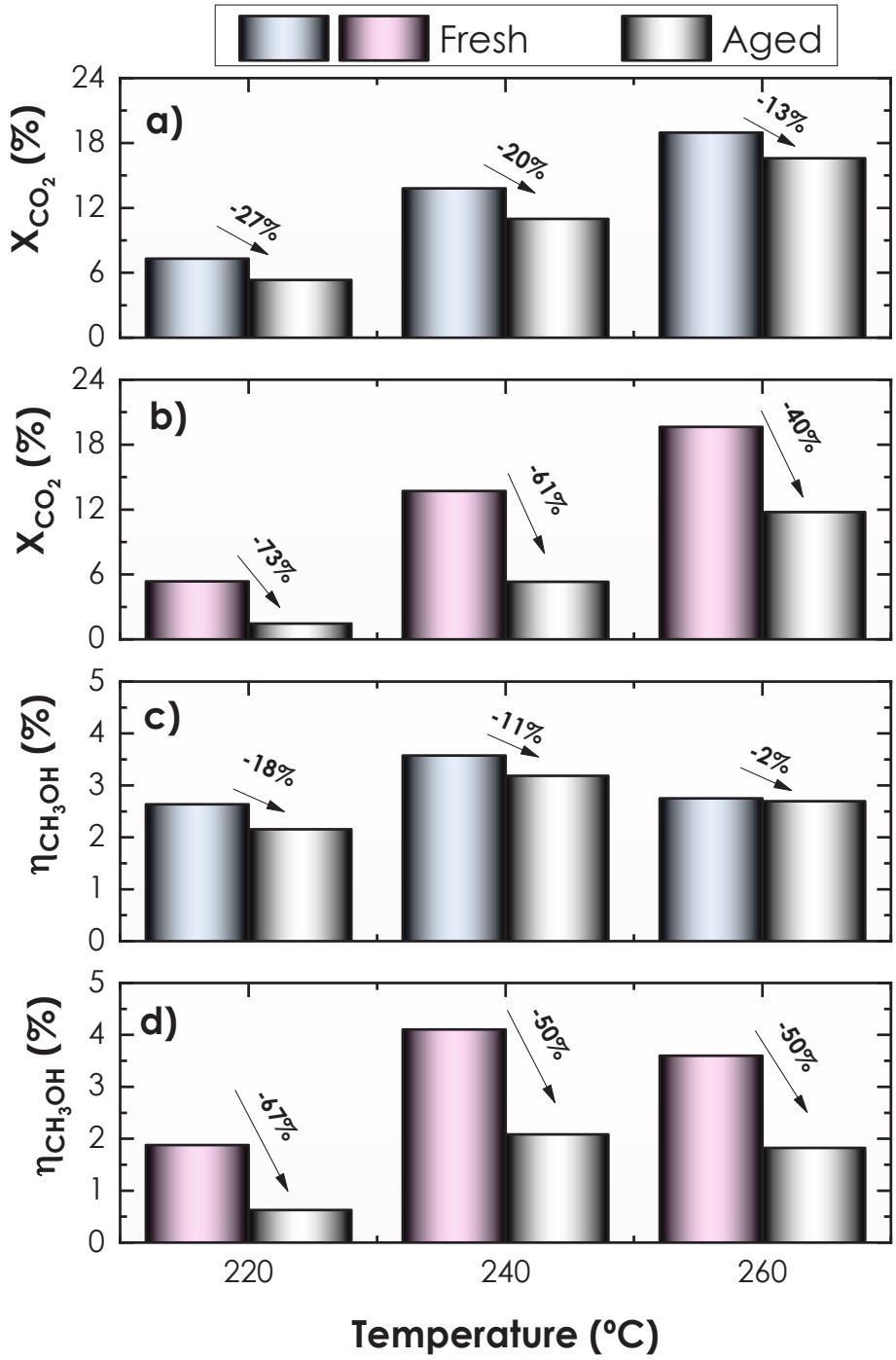

Fig. 7. CO_2 conversion and CH_3OH yield as a function of the temperature (T_{op}) and catalysts history (fresh/aged). (**a**)and (**c**) 10 $\%^{wt}Cu/ZrO_2$ (blue); (**b**) and (**d**) 5 $\%^{wt}Cu$-5 $\%^{wt}Zn/ZrO_2$ (pink); *WHSV* = 6000 $mL_{STP}\ g_{cat}^{-1}h^{-1}$. (For interpretation of the references to colour in this figure legend, the reader is referred to the web version of this article.)

increased, CH_3OH selectivity decreased, indicating that the process approached thermodynamic equilibrium. High CH_3OH selectivity was achieved only at low CO_2 conversion levels, since CO formation became predominant as conversion increased.

The effect of *WHSV* on the process was significant, as operating at high *WHSV* values led to a decrease in CO_2 conversion, which favored process selectivity. The influence of *WHSV* was also temperature-dependent: while a decrease in *WHSV* improved selectivity when the system operated near thermodynamic equilibrium, this trend was not observed at high temperatures (T > 240 °C). At lower temperatures (T = 220 °C), however, this behaviour was evident. At this temperature, the process was far from thermodynamic equilibrium, and increasing the *WHSV* operating temperature caused such a pronounced reduction in CO_2 conversion that the gain in selectivity was offset by the loss in efficiency. Under these conditions, a maximum in selectivity was observed at *WHSV* = 8000 $mL_{STP}\ g_{cat}^{-1}h^{-1}$ (half-full orange rhombuses), attributed to the marked drop in CO_2 conversion.

Fig. 9 shows the evolution of the methanol space–time yield as a function of the operating temperature for different *WHSV* values. The methanol space–time yield STY_{CH3OH} is expressed in g_{Cu}^{-1}, as this unit emphasized the amount of active phase present in the catalytic bed. This choice is particularly relevant given that the present work focuses on

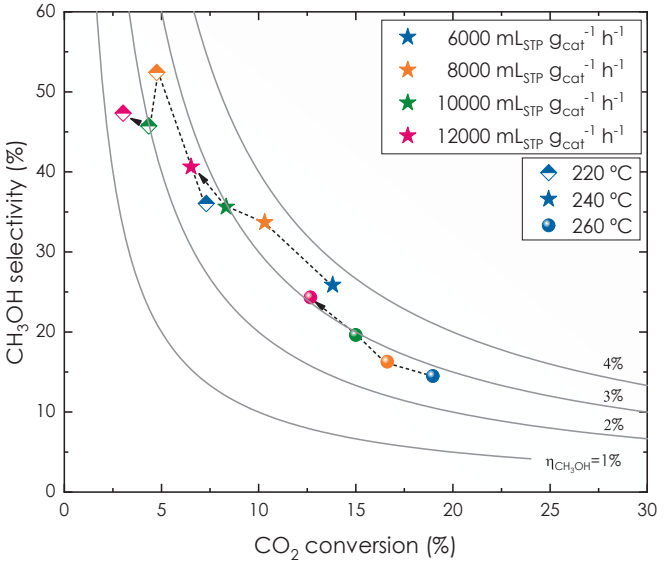

Fig. 8. CH_3OH selectivity as a function of CO_2 conversion. *WHSV* and Temperature (*T*) represented with different colors and symbols, respectively. 10%^{wt}Cu/ZrO_2 catalyst. Dashed lines only for visual guidance (*WHSV* rise).

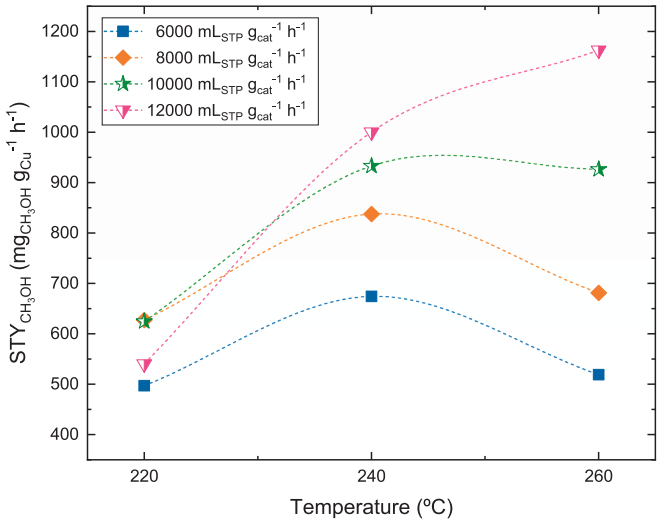

Fig. 9. CH_3OH space–time yield (mg_{CH3OH} $g_{Cu}^{-1}h^{-1}$) as a function of the temperature (*T*). 10 %^{wt}Cu/ZrO_2 catalyst. Dashed lines only for visual guidance (same *WHSV*).

catalysts with a reduced active phase loading and aims to optimize its utilization.

Fig. 9 clearly demonstrates the combined effect of *WHSV* and operating temperature on methanol production, expressed as the methanol space–time yield (STY_{CH3OH}). As previously shown in Fig. 7, the isolated effect of *WHSV* reveals that increasing *WHSV* value leads to a decrease in CO_2 conversion. However, this increase in *WHSV* simultaneously results in an enhancement of CH_3OH production. This behavior can be attributed to the system moving away from thermodynamic equilibrium, allowing higher methanol flow rates as the process is no longer limited by thermodynamic constraints. This phenomenon is reflected in the variation of STY_{CH3OH} with temperature: at low *WHSV* values, where thermodynamic limitations are more pronounced –especially at elevated temperatures- a maximum STY_{CH3OH} is observed at 240 °C. However, as *WHSV* increases, STY_{CH3OH} also increases, broadening the temperature effect. This results in a flattening of the STY_{CH3OH} peak at 240 °C and shift of the maximum towards higher temperatures at elevated *WHSV* values.

A literature review has been conducted on methanol production, focusing on the space–time yield (STY_{CH3OH}) achieved using various copper-based catalyst and operating conditions. The collected data were normalized with respect to the copper content and corrected for residence time (τ) to allow for meaningful comparisons across different studies [79,90–112]. Fig. 10 presents the CH_3OH space–time yield, expressed as mg_{CH3OH} $g_{Cu}^{-1}h^{-1}$, as a function of residence time (τ).

The study presented in Fig. 10 shows the effect of residence time (τ) and the strong influence of the copper mass fraction in the catalyst. Residence time (τ) was a strong dependence on pressure and significantly impacts CH_3OH production, as increasing pressure leads to a proportional increase in residence time (Eq. (6). This increase drives the system closer to thermodynamic equilibrium, thereby reducing the CH_3OH space–time yield (STY_{CH3OH}). Consequently, scaling the process to higher pressures or comparing analytic activities requires a correction of the *WHSV* value, as it is pressure-dependent. This dependency hinders the direct comparison of results obtained at different pressures and further accentuates the constraints imposed by thermodynamic limitations. Fig. 10 shows that methanol production at $\tau > 20$ s was lower than at shorter residence times (as observed in both experimental data and literature), due to the emergence of thermodynamic control at prolonged τ. When the operating pressure is raised and the Weight Hourly Space Velocity (*WHSV*) is simultaneously adjusted to keep the residence time constant (iso- τ) following Eq. (6), rather than holding *WHSV* fixed (*iso-WHSV*), methanol productivity increases sharply. The larger *WHSV* value shortens τ, driving the system further from thermodynamic equilibrium and boosting both methanol selectivity and space–time yield. Under *iso*-τ conditions pressure becomes the sole independent variable; increasing P, for instance from 20 atm to 40 (large stars symbols), elevates the methanol space–time yield (STY_{CH3OH}) to approximately 4 g_{CH3OH} $g_{Cu}^{-1}h^{-1}$, more than double the highest values reported in literature.

The experimental values shown (large stars) in Fig. 10 were higher than those reported in the literature. This discrepancy was attributed to the higher copper mass fraction in the CuO-ZnO-Al_2O_3 catalyst used in the literature (typically 50 ± 10 %^{wt}Cu), compared to the 10 wt.%Cu employed in the present work. Expressing the CH_3OH space–time yield (STY_{CH3OH}) in units of g_{Cu}^{-1} was intended to normalize the analysis to the active phase. This normalization revealed that catalysts with lower copper loading (this work) achieved a more efficient utilization of the active phase compared to conventional CuO-ZnO-Al_2O_3 catalyst.

Methanol space–time yield (STY_{CH3OH}) shows a counter-intuitive trend with single-pass conversion. As operation approaches thermodynamic equilibrium (high τ values), STY_{CH3OH} falls because the equilibrium composition is only weakly selective toward CH_3OH. Conversely, when the process is driven further from equilibrium by lowering τ values, STY_{CH3OH} rises. The overall conclusion is that achieving a high methanol space–time yield (STY_{CH3OH}) requires operating at elevated *WHSV* and temperatures (Figs. 9 and 10).

3.6. Kinetics

As discussed in Section 2.4, three reaction pathways were considered for the evaluation of kinetic parameters. These included: (**i**) the direct hydrogenation of CO_2 to methanol (Reaction r.3), and (**ii**) a stepwise mechanism involving the reverse water–gas shift (rWGS) reaction (Reaction r.2), wherein CO_2 is first converted to CO, followed by methanol synthesis from CO (Reaction r.1). The reaction rate expressions, the adsorption constants and the equilibrium constants were calculated according to the equations 7–15, reported in Table 2.

The kinetic parameters were initially optimized using the 10 %^{wt}Cu/ZrO_2 catalyst under all tested gas hourly space velocity (GHSV) conditions to enable a more robust and comprehensive parameter estimation. As a result, the apparent activation energies were determined to be 106 kJ/mol for r.1, 125 kJ/mol for r.2, and 118 kJ/mol for r.3. The model,

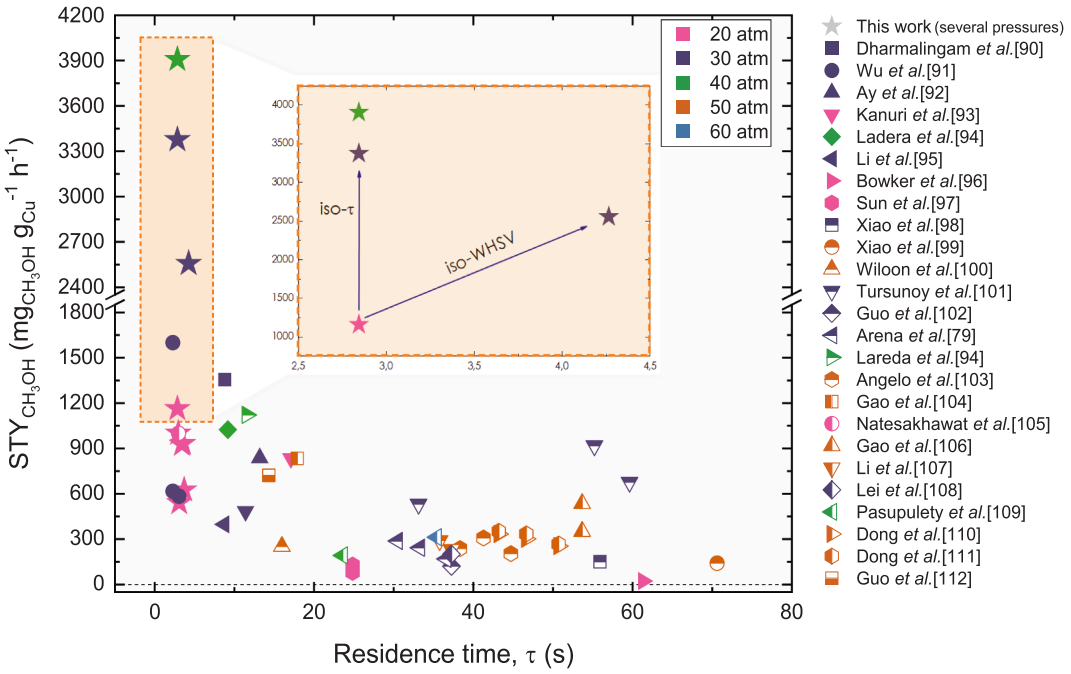

Fig. 10. CH_3OH space–time yield ($mg_{CH3OH}\ g_{Cu}^{-1} h^{-1}$) as a function of the residence time, τ (s). 10 $\%^{wt}Cu/ZrO_2$ catalyst represented in stars symbols. Operating pressure represented with different colors. Data compiled from the literature are represented using different symbols.

incorporating these optimized parameters, exhibited excellent agreement with the experimental data across all conditions, as shown in Fig. 11, thereby validating the model capability to accurately represent a broad range of operating scenarios.

For subsequent kinetic analyses of the other catalyst formulations, the activation energies were fixed at the previously determined values, and only the pre-exponential factors were allowed to vary. The corresponding results are shown in Fig. 12, where the calculated kinetic

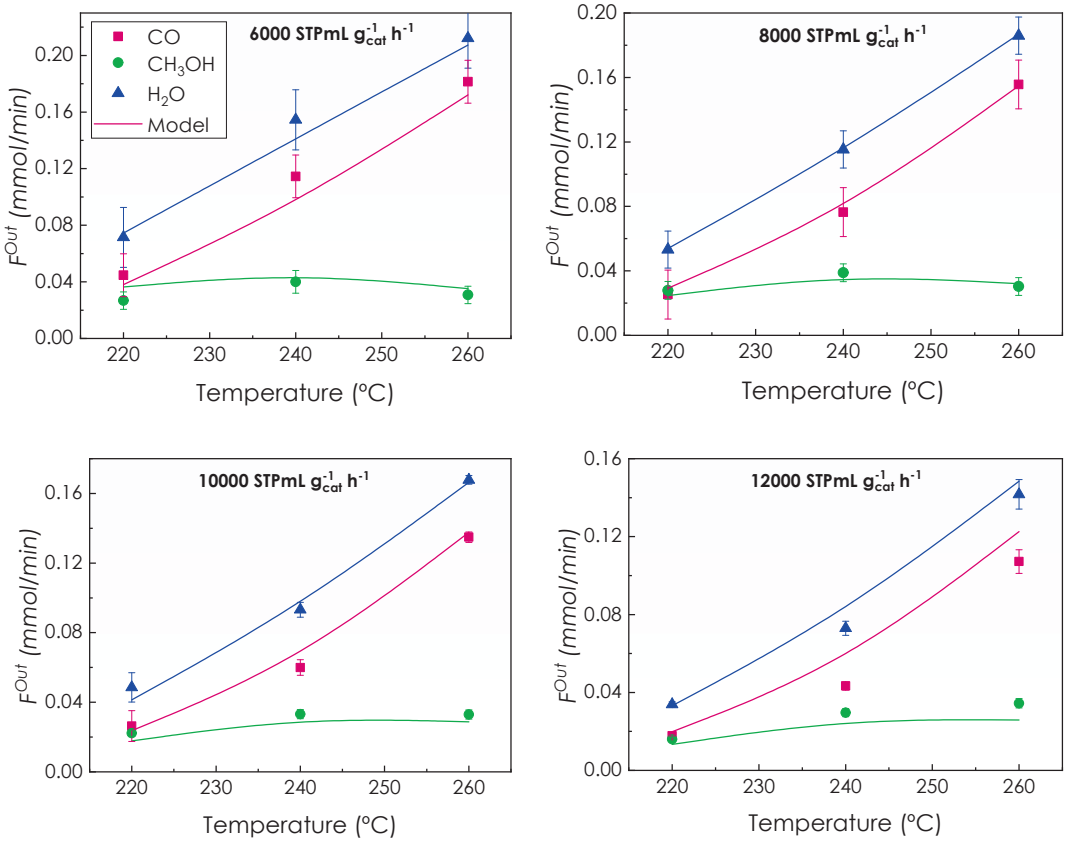

Fig. 11. Comparison between experimental (symbols) and calculated (lines) products molar flowrates (F_i^{Out}, i = CO, CH_3OH, and H_2O) obtained with the catalyst 10 $\%^{wt}Cu/ZrO_2$ in all the *WHSV* operating conditions.

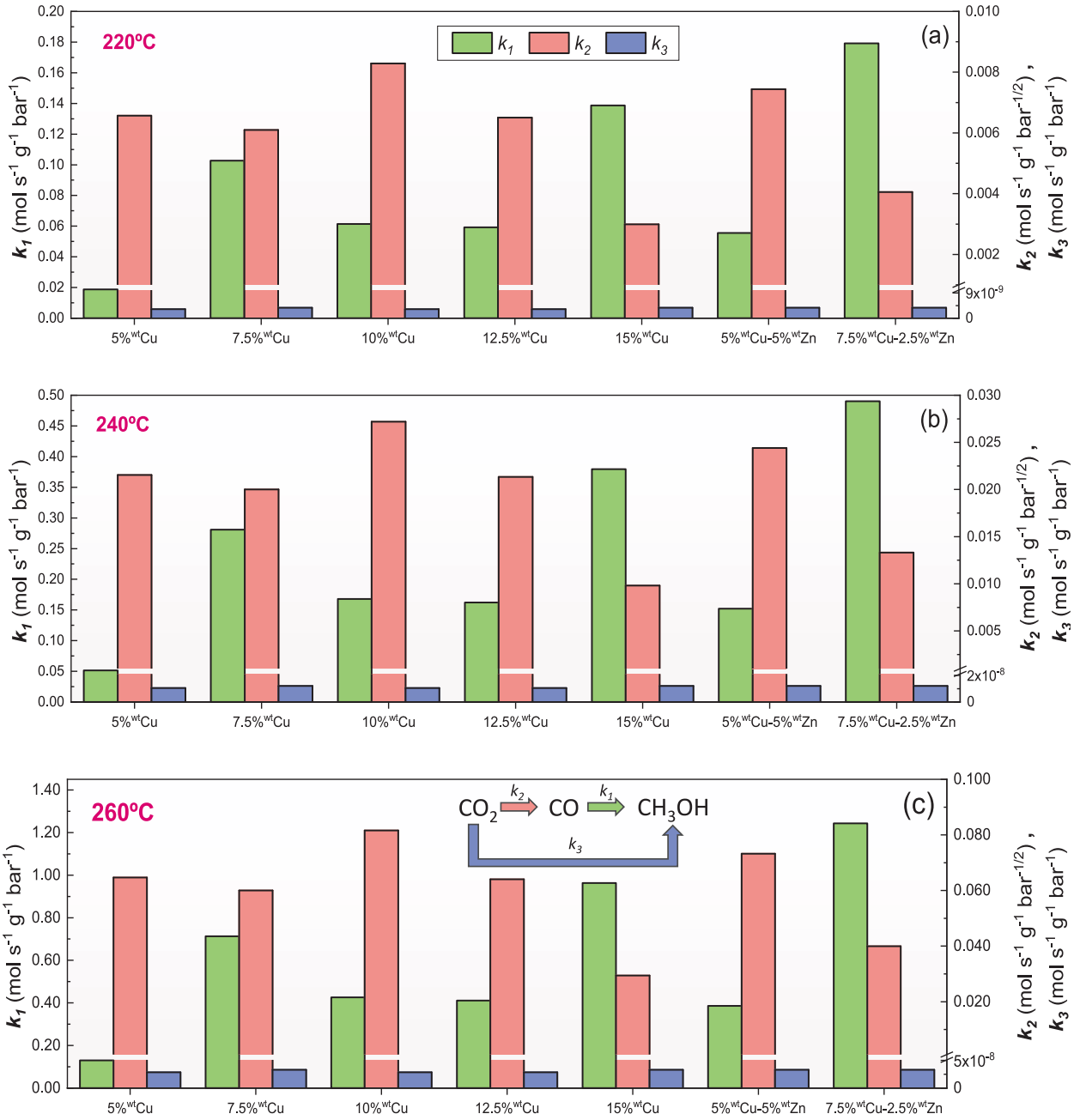

Fig. 12. Kinetic constants calculated for all the catalysts at different temperature: (**a**) 220 °C; (**b**) 240 °C; and (**c**) 260 °C. The values of k_1 must be read on the left Y-axis, while the values of k_2 and k_3 must be read on the right Y-axis.

constants are reported at each temperature. As evidenced, the rate constant for the direct hydrogenation of CO_2 (r.3) is several orders of magnitude lower than those for the stepwise pathway, underscoring the predominance of the latter under the investigated conditions. This evidence clearly outlines how the preferential reaction mechanism for the studied catalysts is the stepwise reaction ($CO_2 \rightarrow CO \rightarrow CH_3OH$), while the direct CO_2 conversion ($CO_2 \rightarrow CH_3OH$) is clearly inhibited.

Furthermore, the kinetic constant for the rWGS reaction (r.2) was consistently lower than that of the CO hydrogenation step (r.1) across all catalysts, indicating that CO_2 activation is the rate-limiting step in the overall process. This suggests that CO formation via *rWGS* is thermodynamically and kinetically favored over the direct generation of reaction intermediates for methanol synthesis. Once CO is formed, its subsequent conversion to methanol proceeds rapidly. The examination of the optimized kinetic constants at the three investigated temperatures revealed no evidence of a mechanistic shift within the studied temperature range, suggesting that the dominant reaction pathway remains consistent across these conditions.

Additionally, this analysis highlights the superior performance of the 10 %^{wt}Cu/ZrO_2 catalyst, which consistently exhibited the highest k_2 value. This observation aligns with experimental performance trends and reinforces the conclusion that the *rWGS* step governs the overall reaction rate. Accordingly, the catalyst that facilitates the fastest CO_2-to-CO conversion demonstrates the highest overall activity for methanol production. Finally, it is possible to observe that the bimetallic formulation 7.5 %^{wt}Cu-2.5 %^{wt}Zn/ZrO_2 always demonstrated the highest k_1 kinetic constant, thus indicating that this catalyst outperformed the others in the promotion of CO to methanol conversion, indicating that Cu/Zn interfaces can be used to tune methanol production. Nevertheless, since CO formation was hindered for this formulation, its overall

performance in CO_2 hydrogenation remained limited by the sluggish rWGS step, highlighting the importance of balancing both CO generation and conversion steps when designing efficient methanol synthesis catalysts.

4. Conclusions

The optimal copper-based catalyst evaluated in this study, 10 $\%^{wt}Cu/ZrO_2$, exhibits high catalytic activity. At T = 260 °C and *WHSV* = 6000 $mL_{STP}\ g_{cat}^{-1}h^{-1}$ thermodynamic control of the reaction is observed. Once the optimal active phase loading (10 wt%) was established, the introduction of a small mass fraction of zinc modified the catalysts activity profile. Especially, Zn addition decrease catalytic activity at low temperatures, while enhancing it at high temperatures. A Cu/Zn mass ratio of 1:1 resulted in the highest CH_3OH yield observed in this work.

Catalysts subjected to an aging test exhibited partial deactivation, with a significant decrease in CO_2 conversion. However, the methanol yield was less affected, leading to an increase in CH_3OH selectivity compared to the fresh catalyst. The 5 $\%^{wt}Cu$-5 $\%^{wt}Zn/ZrO_2$ catalyst showed more pronounced hydrothermal deactivation than the 10 $\%^{wt}Cu/ZrO_2$ catalyst, attributed to the higher susceptibility of ZnO to steam-induced sintering.

The CO_2 hydrogenation to methanol exhibited a strong correlation between CO_2 conversion and CH_3OH selectivity. As the CO_2 conversion approaches thermodynamic equilibrium, CH_3OH selectivity decreased. Conversely, when CO_2 conversion is low CH_3OH selectivity increase.

Increasing the *WHSV* enhances the selectivity when the system operates near thermodynamic equilibrium. However, under conditions far from equilibrium, excessive *WHSV* may lead to a decrease in CH_3OH selectivity. In this case, the gain in CH_3OH selectivity due to the increased *WHSV* value is counterbalanced by the associated decrease in CO_2 conversion.

A strong synergy exixts between operating temperature (*T*) and Weight Hourly Space Velocity (*WHSV*), whereby the negative effect of increasing temperature-associated with a reduction in thermodynamic conversion limit is counterbalanced by higher *WHSV* values, which drive the system further from equilibrium. As a result, CH_3OH production, expressed as the methanol space–time yield (STY_{CH3OH}), increases with *WHSV*, effectively mitigating thermodynamic constraints due to the lower proximity of the process to equilibrium conditions.

Elevating the operating pressure (*P*) inevitably alters the residence time (τ) for a fixed Weight Hourly Space Velocity (*WHSV*) value, because a higher *P* compresses the gas phase. Besides widening the thermodynamic equilibrium for methanol synthesis, this pressure increase also allows a proportionally larger volumetric feed. Experimentally two strategies arise when the pressure is raised from a lower value: (**i**) keep *WHSV* constant (*iso-WHSV*) or (**ii**) readjust *WHSV* value to restore the original τ (iso- τ). The data showed that methanol space–time yield (STY_{CH3OH}) is maximized at shorter τ; hence, to capitalize on the beneficial effect of higher pressure, *WHSV* value must be increased accordingly to maintain a low τ and thus sustain high methanol production.

The catalyst proposed in this work (10 $\%^{wt}Cu/ZrO_2$), that is characterized by its low active-phase mass loading, exhibited a (STY_{CH3OH}) CH_3OH space–time yield per gram of copper higher than that of conventional CuO-ZnO-Al_2O_3 catalyst (with a higher copper loading composition). This result demonstrates a cost-effective catalytic methodology, featuring high catalytic activity and optimal utilization of the active phase.

CRediT authorship contribution statement

R. González-Pizarro: Writing – original draft, Visualization, Software, Methodology, Investigation, Formal analysis, Data curation. **S. Renda:** Writing – original draft, Software, Methodology, Formal analysis, Data curation, Conceptualization. **J. Lasobras:** Methodology, Investigation, Data curation, Conceptualization. **J. Soler:** Writing – review & editing, Validation, Supervision, Resources, Project administration, Funding acquisition, Conceptualization. **M. Menéndez:** Writing – review & editing, Validation, Supervision, Resources, Project administration, Funding acquisition, Conceptualization. **J. Herguido:** Writing – review & editing, Visualization, Supervision, Methodology, Conceptualization.

Declaration of competing interest

The authors declare that they have no known competing financial interests or personal relationships that could have appeared to influence the work reported in this paper.

Acknowledgements

The consolidated research group Catalysis and Reactor Engineering Group (CREG, T43–23R) has the financial support of Gobierno de Aragón through the European Social Fund – FEDER.

Financial support from *Agencia Española de Investigación* (Projects PDC2022-133066-I00/AEI/10.13039/501100011033 and PID2022-139819OB-I00), with financial support from the European Union "NextGeneration EU"/PRTR and European Union Fund for Recovery and Resilience are gratefully acknowledged.

R. González-Pizarro wants to express his gratitude for the research grant of *Ministerio de Ciencia e Innovación* of the Spanish Government (grant no. PRE3023-UZ-26).

R. González-Pizarro wishes to express his sincere gratitude to the Sociedad Española de Catálisis (SECAT) for the funding provided through the Programa de Movilidad, and to R. Calero-Berrocal and C. Prieto from MOEVE for facilitating the national research stay at the Centro de Innovación para la Transición Energética (CITE).

S.R. acknowledges the funding of the *Juan de la Cierva* fellowship (grant no. JDC2023-052947-I) by MCIU/AEI/10.13039/501100011033 and FSE + .

Finally, authors would like to acknowledge the use of *Servicio General de Apoyo a la Investigación*-SAI, *and the use of instrumentation as well as the technical advice provided by the National Facility* ELECMI ICTS, node *Laboratorio de Microscopias Avanzadas (LMA) at* Universidad de Zaragoza.

Data availability

Data will be made available on request.

References

[1] Anderson TR, Hawkins E, Jones PD. CO_2, the greenhouse effect and global warming: from the pioneering work of Arrhenius and Callendar to today's Earth System Models. Endeavour 2016;40:178–87. https://doi.org/10.1016/j.endeavour.2016.07.002.

[2] Akhmetshin MR, Nyashina GS, Strizhak PA. Normalizing anthropogenic gas emissions from the combustion of industrial waste as part of fuel slurries. Fuel 2022;313. https://doi.org/10.1016/j.fuel.2021.122653.

[3] Akpolat AG, Bakırtaş T. The nonlinear impact of renewable energy, fossil energy and CO_2 emissions on human development index for the eight developing countries. Energy 2024;312. https://doi.org/10.1016/j.energy.2024.133466.

[4] Filonchyk M, Peterson MP, Zhang L, Hurynovich V, He Y. Greenhouse gases emissions and global climate change: Examining the influence of CO_2, CH_4, and N_2O. Sci Total Environ 2024;935. https://doi.org/10.1016/j.scitotenv.2024.173359.

[5] S. Sivaramanan, Global Warming and Climate change, causes, impacts and mitigation, (n.d.). Doi: 10.13140/RG.2.1.4889.7128.

[6] IPCC, Global Warming of 1.5°C, Cambridge University Press, 2022. Doi: 10.1017/9781009157940.

[7] Friedlingstein P, et al. Global Carbon Budget 2024;2024. https://doi.org/10.5194/essd-2024-519.

[8] Kabir M, Habiba UE, Khan W, Shah A, Rahim S, los Rios-Escalante PRD, Farooqi ZUR, Ali L. Climate change due to increasing concentration of carbon dioxide and its impacts on environment in 21st century; a mini review. J King Saud Univ Sci 2023;35. https://doi.org/10.1016/j.jksus.2023.102693.

[9] Rothenberg G. A realistic look at CO_2 emissions, climate change and the role of sustainable chemistry. Sustainable Chem Clim Action 2023;2. https://doi.org/10.1016/j.scca.2023.100012.

[10] Yuan X, Bai X, Zhou Z, Luo G, Li J, Ran C, et al. Global impacts of land use on terrestrial carbon emissions since 1850. Sci Total Environ 2025;963. https://doi.org/10.1016/j.scitotenv.2024.178358.

[11] Nabera A, Istrate IR, Martín AJ, Pérez-Ramírez J, Guillén-Gosálbez G. Energy crisis in Europe enhances the sustainability of green chemicals. Green Chem 2023;25:6603–11. https://doi.org/10.1039/d3gc01053h.

[12] Lee K, Liu X, Vyawahare P, Sun P, Elgowainy A, Wang M. Techno-economic performances and life cycle greenhouse gas emissions of various ammonia production pathways including conventional, carbon-capturing, nuclear-powered, and renewable production. Green Chem 2022;24:4830–44. https://doi.org/10.1039/d2gc00843b.

[13] Olah GA, Goeppert A, Prakash GKS. Chemical recycling of carbon dioxide to methanol and dimethyl ether: from greenhouse gas to renewable, environmentally carbon neutral fuels and synthetic hydrocarbons. J Org Chem 2009;74:487–98. https://doi.org/10.1021/jo801260f.

[14] Perathoner S, Centi G. CO_2 recycling: a key strategy to introduce green energy in the chemical production chain. ChemSusChem 2014;7:1274–82. https://doi.org/10.1002/cssc.201300926.

[15] Martínez JD, Sanchís A, Veses A, Kapf A, López JM, Callén MS, et al. Waste-based value-added feedstocks from tire pyrolysis oil distillation: defossilization of the petrochemical industry. Green Chem 2024. https://doi.org/10.1039/d4gc05185h.

[16] Ahmed S, Khan MK, Kim J. Revolutionary advancements in carbon dioxide valorization via metal-organic framework-based strategies. Carbon Capture Science and Technology 2025;15. https://doi.org/10.1016/j.ccst.2025.100405.

[17] Bhattacharyya R, Gupta A, Venkataraman S. Efficient fuel conversion for power generation under distributed solar generation and carbon emission regulations. Electricity Journal 2016;29:48–61. https://doi.org/10.1016/j.tej.2016.06.002.

[18] Martins F, Moura P, de Almeida AT. The role of electrification in the decarbonization of the energy sector in portugal. Energies (Basel) 2022;15. https://doi.org/10.3390/en15051759.

[19] Szima S, Cormos CC. Improving methanol synthesis from carbon-free H2 and captured CO2: a techno-economic and environmental evaluation. J CO2 Util 2018;24:555–63. https://doi.org/10.1016/j.jcou.2018.02.007.

[20] Machaj K, Kupecki J, Malecha Z, Morawski AW, Skrzypkiewicz M, Stanclik M, et al. Ammonia as a potential marine fuel: a review. Energ Strat Rev 2022;44. https://doi.org/10.1016/j.esr.2022.100926.

[21] Herbinet O, Bartocci P, Grinberg Dana A. On the use of ammonia as a fuel – a perspective. Fuel Commun 2022;11:100064. https://doi.org/10.1016/j.jfueco.2022.100064.

[22] Blanco EC, Sánchez A, Martín M, Vega P. Methanol and ammonia as emerging green fuels: evaluation of a new power generation paradigm. Renew Sustain Energy Rev 2023;175. https://doi.org/10.1016/j.rser.2023.113195.

[23] Van Der Giesen C, Kleijn R, Kramer GJ. Energy and climate impacts of producing synthetic hydrocarbon fuels from CO_2. Environ Sci Technol 2014;48:7111–21. https://doi.org/10.1021/es500191g.

[24] Martin O, Pérez-Ramírez J. New and revisited insights into the promotion of methanol synthesis catalysts by CO_2. Cat Sci Technol 2013;3:3343–52. https://doi.org/10.1039/c3cy00573a.

[25] Pérez-ramírez J, Mondelli SC, Guillén-gosálbez G, Pérez-ramírez J, Mondelli C, Guille G. Showcasing collaborative research from the groups of As featured. Energy & Environmental Science B 2019. https://doi.org/10.1039/c9ee01673b.

[26] Khan MK, Ahmed S, Bibi SS, Helaley A, Liang X, Kim J. Advances in CO_2 hydrogenation: mechanisms and catalysts for alcohol synthesis. Chem Eng J 2025;517. https://doi.org/10.1016/j.cej.2025.164209.

[27] Ahmed S, Hussain MS, Khan MK, Kim J. Innovations in catalysis towards efficient electrochemical reduction of CO_2 to C_1 chemicals. Journal of Energy Chemistry 2025;107:622–49. https://doi.org/10.1016/j.jechem.2025.03.055.

[28] Olah GA. Beyond oil and gas: the methanol economy. Angewandte Chemie - International Edition 2005;44:2636–9. https://doi.org/10.1002/anie.200462121.

[29] Schlögl R. Chemical energy storage enables the transformation of fossil energy systems to sustainability. Green Chem 2021;23:1584–93. https://doi.org/10.1039/d0gc03171b.

[30] Minten H, Vandegehuchte BD, Jaumard B, Meys R, Reinert C, Bardow A. Early-stage impact assessment tool (ESTIMATe) for the life cycle assessment of CO_2-based chemicals. Green Chem 2024;26:8728–43. https://doi.org/10.1039/d4gc00964a.

[31] Mondal U, Yadav GD. Methanol economy and net zero emissions: critical analysis of catalytic processes, reactors and technologies. Green Chem 2021;23:8361–405. https://doi.org/10.1039/d1gc02078a.

[32] Pio DT, Vilas-Boas ACM, Rodrigues NFC, Mendes A. Carbon neutral methanol from pulp mills towards full energy decarbonization: an inside perspective and critical review. Green Chem 2022;24:5403–28. https://doi.org/10.1039/d2gc01528e.

[33] Sternberg A, Jens CM, Bardow A. Life cycle assessment of CO_2-based C_1-chemicals. Green Chem 2017;19:2244–59. https://doi.org/10.1039/c6gc02852g.

[34] Renda S, Menéndez M. Process intensification for CO_2 hydrogenation to liquid fuels. Catalysts 2025;15:509. https://doi.org/10.3390/catal15060509.

[35] He J, Tian G, Liao D, Li Z, Cui Y, Wei F, et al. Mechanistic insights into methanol conversion and methanol-mediated tandem catalysis toward hydrocarbons. Journal of Energy Chemistry 2026;112:778–803. https://doi.org/10.1016/j.jechem.2025.09.007.

[36] González-Pizarro R, Calero-Berrocal R, Lasobras J, Renda S, Rodríguez-Pardo MR, Soler J, et al. Tuning e-fuel selectivity in sorption-enhanced CO_2 hydrogenation over In_2O_3/ZrO_2: the effect of LTA and FAU zeolites. Fuel 2026;406. https://doi.org/10.1016/j.fuel.2025.136974.

[37] Bicer Y, Dincer I. Environmental impact categories of hydrogen and ammonia driven transoceanic maritime vehicles: a comparative evaluation. Int J Hydrogen Energy 2018;43:4583–96. https://doi.org/10.1016/j.ijhydene.2017.07.110.

[38] Dieterich V, Buttler A, Hanel A, Spliethoff H, Fendt S. Power-to-liquid via synthesis of methanol, DME or Fischer–Tropsch-fuels: a review. Energy Environ Sci 2020;13:3207–52. https://doi.org/10.1039/d0ee01187h.

[39] Jadhav SG, Vaidya PD, Bhanage BM, Joshi JB. Catalytic carbon dioxide hydrogenation to methanol: a review of recent studies. Chem Eng Res Des 2014;92:2557–67. https://doi.org/10.1016/j.cherd.2014.03.005.

[40] Bos MJ, Kersten SRA, Brilman DWF. Wind power to methanol: Renewable methanol production using electricity, electrolysis of water and CO_2 air capture. Appl Energy 2020;264. https://doi.org/10.1016/j.apenergy.2020.114672.

[41] K. Andersson, C.M. Salazar, Methanol As A Marine Fuel Report 2015.

[42] Dias V, Pochet M, Contino F, Jeanmart H. Energy and economic costs of chemical storage. Front Mech Eng 2020;6. https://doi.org/10.3389/fmech.2020.00021.

[43] DeSantis D, James BD, Houchins C, Saur G, Lyubovsky M. Cost of long-distance energy transmission by different carriers. IScience 2021;24. https://doi.org/10.1016/j.isci.2021.103495.

[44] Al-Breiki M, Bicer Y. Comparative cost assessment of sustainable energy carriers produced from natural gas accounting for boil-off gas and social cost of carbon. Energy Rep 2020;6:1897–909. https://doi.org/10.1016/j.egyr.2020.07.013.

[45] Shi D, Heyte S, Capron M, Paul S. Catalytic processes for the direct synthesis of dimethyl carbonate from CO2and methanol: a review. Green Chem 2022;24:1067–89. https://doi.org/10.1039/d1gc04093f.

[46] Wang L, Jin J, Li W, Li C, Zhu L, Zhou Z, et al. Highly selective catalytic oxidation of methane to methanol using Cu-Pd/anatase. Energy Environ Sci 2024. https://doi.org/10.1039/d4ee02671c.

[47] Artz J, Müller TE, Thenert K, Kleinekorte J, Meys R, Sternberg A, et al. Sustainable conversion of carbon dioxide: an integrated review of catalysis and life cycle assessment. Chem Rev 2018;118:434–504. https://doi.org/10.1021/acs.chemrev.7b00435.

[48] Zhang D, Wang R, Zhang Z, Yan H, Zhou X, Zhao H, et al. Industrial ultra-low-carbon methanol synthesis routes: techno-economic analysis, life cycle environment assessment and multi-dimensional sustainability evaluation. Green Chem 2025. https://doi.org/10.1039/d4gc05482b.

[49] Guo P, Xue R, Zou Q, Ma X, Su C, Zeng Z, et al. Enhanced ultramicropore of biomass-derived porous carbon for efficient and low-energy CO_2 capture: integration of adsorption and solar desorption. Energy Environ Mater 2025. https://doi.org/10.1002/eem2.70140.

[50] Szczygieł J, Kułażyński M. Thermodynamic limitations of synthetic fuel production using carbon dioxide: a cleaner methanol-to-gasoline process. J Clean Prod 2020;276. https://doi.org/10.1016/j.jclepro.2020.122790.

[51] J. Skrzypek, M. Lachowska, M. Grzesik, J. Sj; Oczy&ki, P. Nowak, Thermodynamics and kinetics of low pressure methanol synthesis, 1995.

[52] W.-J. Shen, K.-W. Jun, H.-S. Choi, K.-W. Lee, Thermodynamic Investigation of Methanol and Dimethyl Ether Synthesis from CO_2 Hydrogenation, 2000.

[53] Ateka A, Pérez-Uriarte P, Gamero M, Ereña J, Aguayo AT, Bilbao J. A comparative thermodynamic study on the CO_2 conversion in the synthesis of methanol and of DME. Energy 2017;120:796–804. https://doi.org/10.1016/j.energy.2016.11.129.

[54] van Bennekom JG, Venderbosch RH, Winkelman JGM, Wilbers E, Assink D, Lemmens KPJ, et al. Methanol synthesis beyond chemical equilibrium. Chem Eng Sci 2013;87:204–8. https://doi.org/10.1016/j.ces.2012.10.013.

[55] B.A.T. Mehrabadi, S. Eskandari, U. Khan, R.D. White, J.R. Regalbuto, A Review of Preparation Methods for Supported Metal Catalysts, in: Advances in Catalysis, Academic Press Inc., 2017: pp. 1–35. Doi: 10.1016/bs.acat.2017.10.001.

[56] "Chapter 9 Preparation of supported catalysts," in Studies in surface science and catalysis, 1993, pp. 335–360. doi: 10.1016/s0167-2991(08)63813-6.

[57] Cao P, Long M, Zheng X, Zhou C, Chen Y, Rittmann BE. Selective regulation of product generation from CO_2 hydrogenation on Pd-based catalysts: a critical review from a pathway perspective. Energy & Environmental Sustainability 2025;1:100020. https://doi.org/10.1016/j.eesus.2025.100020.

[58] Behrens M. Heterogeneous catalysis of CO_2 conversion to methanol on copper surfaces. Angewandte Chemie - International Edition 2014;53:12022–4. https://doi.org/10.1002/anie.201409282.

[59] Liu Y, Zhang Y, Wang T, Tsubaki N. Efficient conversion of carbon dioxide to methanol using copper catalyst by a new low-temperature hydrogenation process. Chem Lett 2007;36:1182–3. https://doi.org/10.1246/cl.2007.1182.

[60] Bolívar Caballero JJ, Zaini IN, Yang W. Reforming processes for syngas production: a mini-review on the current status, challenges, and prospects for biomass conversion to fuels. Appl Energy Combust Sci 2022;10. https://doi.org/10.1016/j.jaecs.2022.100064.

[61] Azhari NJ, Erika D, Mardiana S, Ilmi T, Gunawan ML, Makertihartha IGBN, et al. Methanol synthesis from CO_2: a mechanistic overview. Results Eng 2022;16:100711. https://doi.org/10.1016/j.rineng.2022.100711.

[62] Kurtz M, Wilmer H, Genger T, Hinrichsen O, Muhler M. Deactivation of supported copper catalysts for methanol synthesis. Catal Lett 2003;86(1–3):77–80. https://doi.org/10.1023/a:1022663125977.

[63] Fichtl MB, Schlereth D, Jacobsen N, Kasatkin I, Schumann J, Behrens M, et al. Kinetics of deactivation on $Cu/ZnO/Al_2O_3$ methanol synthesis catalysts. Appl Catal A 2015;502:262–70. https://doi.org/10.1016/j.apcata.2015.06.014.

[64] Sun JT, Metcalfe IS, Sahibzada M. Deactivation of $Cu/ZnO/Al_2O_3$ methanol synthesis catalyst by sintering. Ind Eng Chem Res 1999;38:3868–72. https://doi.org/10.1021/ie990078s.

[65] Song K, Feng X, Ju X, Ma D, Wang S, Shi JW. Poisoning mechanism of potassium and calcium on a Mn-based quasi-MOF de-NOx catalyst. J Hazard Mater 2025;497. https://doi.org/10.1016/j.jhazmat.2025.139714.

[66] Sun Y, Zhu Y, Xin T, Li X, Zhou X, Bai G, et al. Preparation modification and water resistance optimization of Cu-Mn CO catalyst. Appl Surf Sci 2025;708. https://doi.org/10.1016/j.apsusc.2025.163768.

[67] Zhu D, Li M, Wu Z, Du Y, Luo B, Huang P, et al. Copper-catalyzed one-pot synthesis of dibenzofurans, xanthenes, and xanthones from cyclic diphenyl iodoniums. European J Org Chem 2019;2019:4566–71. https://doi.org/10.1002/ejoc.201900745.

[68] González-Pizarro R, Lasobras J, Soler J, Herguido J, Menéndez M. Proof of concept for a sorption-enhanced reactor with continuous sorbent feeding (CSF): application to green methanol production. Chem Eng J 2025;517:164562. https://doi.org/10.1016/j.cej.2025.164562.

[69] Trifan B, Lasobras J, Soler J, Herguido J, Menéndez M. Modifications in the composition of $CuO/ZnO/Al_2O_3$ catalyst for the synthesis of methanol by CO_2 hydrogenation. Catalysts 2021;11. https://doi.org/10.3390/catal11070774.

[70] Liang B, Ma J, Su X, Yang C, Duan H, Zhou H, et al. Investigation on deactivation of $Cu/ZnO/Al_2O_3$ catalyst for CO_2 hydrogenation to methanol. Ind Eng Chem Res 2019;58:9030–7. https://doi.org/10.1021/acs.iecr.9b01546.

[71] Twigg MV, Spencer MS. Deactivation of copper metal catalysts for methanol decomposition, methanol steam reforming and methanol synthesis. Top Catal 2003;22(3–4):191–203. https://doi.org/10.1023/a:1023567718303.

[72] Li D, Wang Z, Jin S, Zhu M. Deactivation and regeneration of the commercial $Cu/ZnO/Al_2O_3$ catalyst in low-temperature methanol steam reforming. Sci China Chem 2023;66:3645–52. https://doi.org/10.1007/s11426-023-1789-3.

[73] Graaf GH, Stamhuis EJ, Beenackers AACM. Kinetics of low-pressure methanol synthesis. Chem Eng Sci 1988;43(12):3185–95. https://doi.org/10.1016/0009-2509(88)85127-3.

[74] Van Kampen J, Boon J, Vente J, Van Sint Annaland M. Sorption enhanced dimethyl ether synthesis under industrially relevant conditions: experimental validation of pressure swing regeneration. React Chem Eng 2021;6:244–57. https://doi.org/10.1039/d0re00431f.

[75] Haryanto A, Fernando SD, Filip To SD, Steele PH, Pordesimo L. High temperature water gas shift reaction over nickel catalysts for hydrogen production: effect of supports, GHSV, metal loading, and dopant materials. J Thermodyn Catal 2011;02. https://doi.org/10.4172/2157-7544.1000106.

[76] Vu TTN, Desgagnés A, Iliuta MC. Efficient approaches to overcome challenges in material development for conventional and intensified CO_2 catalytic hydrogenation to CO, methanol, and DME. Appl Catal A 2021;617. https://doi.org/10.1016/j.apcata.2021.118119.

[77] Zhou G, Xie F, Deng L, Zhang G, Xie H. Supported mesoporous Cu/CeO_2-δ catalyst for CO_2 reverse water–gas shift reaction to syngas. Int J Hydrogen Energy 2020;45:11380–93. https://doi.org/10.1016/j.ijhydene.2020.02.058.

[78] Ren H, Xu CH, Zhao HY, Wang YX, Liu J, Liu JY. Methanol synthesis from CO_2 hydrogenation over Cu/γ-Al_2O_3 catalysts modified by ZnO, ZrO_2 and MgO. J Ind Eng Chem 2015;28:261–7. https://doi.org/10.1016/j.jiec.2015.03.001.

[79] Arena F, Barbera K, Italiano G, Bonura G, Spadaro L, Frusteri F. Synthesis, characterization and activity pattern of $Cu-ZnO/ZrO_2$ catalysts in the hydrogenation of carbon dioxide to methanol. J Catal 2007;249:185–94. https://doi.org/10.1016/j.jcat.2007.04.003.

[80] Dalebout R, Barberis L, Totarella G, Turner SJ, La Fontaine C, De Groot FMF, et al. Insight into the nature of the ZnO_x promoter during methanol synthesis. ACS Catal 2022;12:6628–39. https://doi.org/10.1021/acscatal.1c05101.

[81] Mota N, Guil-Lopez R, Pawelec BG, Fierro JLG, Navarro RM. Highly active Cu/ZnO-Al catalyst for methanol synthesis: effect of aging on its structure and activity. RSC Adv 2018;8:20619–29. https://doi.org/10.1039/c8ra03291b.

[82] Zeng X, Zhang A, Liu C, Cheng J, Hu M. Helical polyether-immobilized chiral aza-bis(oxazolines): synthesis and synergistic effect on the enantioselectivity of Zn-catalyzed Henry reaction. Eur Polym J 2023;194. https://doi.org/10.1016/j.eurpolymj.2023.112160.

[83] Walter D, Hackebeil J, Hübler C, Schumann E, Lißner A, Störr B, et al. Deactivation of $Cu/ZnO/Al_2O_3$ catalysts by sintering in liquid phase assisted methanol synthesis from CO_2/H_2 and a way to counteract it. J Catal 2024;440. https://doi.org/10.1016/j.jcat.2024.115829.

[84] Etim UJ, Song Y, Zhong Z. Improving the Cu/ZnO-based catalysts for carbon dioxide hydrogenation to methanol, and the use of methanol as a renewable energy storage media. Front Earth Sci (Lausanne) 2020;8. https://doi.org/10.3389/fenrg.2020.545431.

[85] Salami R, Zeng Y, Han X, Rohani S, Zheng Y. Exploring catalyst developments in heterogeneous CO_2 hydrogenation to methanol and ethanol: a journey through reaction pathways. Journal of Energy Chemistry 2025;101:345–84. https://doi.org/10.1016/j.jechem.2024.08.069.

[86] Merte LR, Peng G, Bechstein R, Rieboldt F, Farberow CA, Grabow LC, et al. Water-mediated proton hopping on an iron oxide surface. Science 1979;336(2012):889–93. https://doi.org/10.1126/science.1219468.

[87] Studt F, Behrens M, Kunkes EL, Thomas N, Zander S, Tarasov A, et al. The mechanism of CO and CO_2 hydrogenation to methanol over Cu-based catalysts. ChemCatChem 2015;7:1105–11. https://doi.org/10.1002/cctc.201500123.

[88] Grabow LC, Mavrikakis M. Mechanism of methanol synthesis on cu through CO_2 and CO hydrogenation. ACS Catal 2011;1:365–84. https://doi.org/10.1021/cs200055d.

[89] Martin O, Martín AJ, Mondelli C, Mitchell S, Segawa TF, Hauert R, et al. Indium oxide as a superior catalyst for methanol synthesis by CO_2 hydrogenation. Angewandte Chemie - International Edition 2016;55:6261–5. https://doi.org/10.1002/anie.201600943.

[90] Dharmalingam BC, Koushik V A, Mureddu M, Atzori L, Lai S, Pettinau A, Kaisare NS, Aghalayam P, Varghese JJ. Unravelling the role of metal-metal oxide interfaces of $Cu/ZnO/ZrO_2/Al_2O_3$ catalyst for methanol synthesis from CO_2: Insights from experiments and DFT-based microkinetic modeling. Appl Catal B 332 2023. https://doi.org/10.1016/j.apcatb.2023.122743.

[91] Wu C, Lin L, Liu J, Zhang J, Zhang F, Zhou T, et al. Inverse ZrO_2/Cu as a highly efficient methanol synthesis catalyst from CO_2 hydrogenation. Nat Commun 2020;11. https://doi.org/10.1038/s41467-020-19634-8.

[92] Ay S, Ozdemir M, Melikoglu M. Effects of metal promotion on the performance, catalytic activity, selectivity and deactivation rates of $Cu/ZnO/Al_2O_3$ catalysts for methanol synthesis. Chem Eng Res Des 2021;175:146–60. https://doi.org/10.1016/j.cherd.2021.08.039.

[93] Kanuri S, Singh SA, Dinda S. Prominence of Fe on $Cu/ZnO/ZrO_2$ catalyst for methanol synthesis from CO_2: material preparation, performance demonstration, and kinetic analysis. Chem Eng Sci 2024;286:119661. https://doi.org/10.1016/j.ces.2023.119661.

[94] Ladera R, Pérez-Alonso FJ, González-Carballo JM, Ojeda M, Rojas S, Fierro JLG. Catalytic valorization of CO_2 *via* methanol synthesis with Ga-promoted Cu-ZnO-ZrO_2 catalysts. Appl Catal B 2013;142–143:241–8. https://doi.org/10.1016/j.apcatb.2013.05.019.

[95] Li Z, Du T, Li Y, Jia H, Wang Y, Song Y, et al. Water- and reduction-free preparation of oxygen vacancy rich Cu-ZnO-ZrO_2 catalysts for promoted methanol synthesis from CO_2. Fuel 2022;322. https://doi.org/10.1016/j.fuel.2022.124264.

[96] Bowker M. Methanol synthesis from CO_2 hydrogenation. ChemCatChem 2019;11:4238–46. https://doi.org/10.1002/cctc.201900401.

[97] Sun Q, Zhang Y-L, Chen H-Y, Deng J-F, Wu D, Chen S-Y. A novel process for the preparation of Cu/ZnO and $Cu/ZnO/Al_2O_3$ ultrafine catalyst: structure, surface properties, and activity for methanol synthesis from CO_2+H_2. J Catal 1997;167(1):92–105. https://doi.org/10.1006/jcat.1997.1554.

[98] Xiao J, Mao D, Guo X, Yu J. Effect of TiO_2, ZrO_2, and TiO_2-ZrO_2 on the performance of CuO-ZnO catalyst for CO_2 hydrogenation to methanol. Appl Surf Sci 2015;338:146–53. https://doi.org/10.1016/j.apsusc.2015.02.122.

[99] Xiao S, Zhang Y, Gao P, Zhong L, Li X, Zhang Z, et al. Highly efficient Cu-based catalysts via hydrotalcite-like precursors for CO_2 hydrogenation to methanol. Catal Today 2017;281:327–36. https://doi.org/10.1016/j.cattod.2016.02.004.

[100] Witoon T, Chalorngtham J, Dumrongbunditkul P, Chareonpanich M, Limtrakul J. CO_2 hydrogenation to methanol over Cu/ZrO_2 catalysts: effects of zirconia phases. Chem Eng J 2016;293:327–36. https://doi.org/10.1016/j.cej.2016.02.069.

[101] Tursunov O, Kustov L, Tilyabaev Z. Methanol synthesis from the catalytic hydrogenation of CO_2 over CuO–ZnO supported on aluminum and silicon oxides. J Taiwan Inst Chem Eng 2017;78:416–22. https://doi.org/10.1016/j.jtice.2017.06.049.

[102] Guo X, Mao D, Wang S, Wu G, Lu G. Combustion synthesis of CuO-ZnO-ZrO_2 catalysts for the hydrogenation of carbon dioxide to methanol. Catal Commun 2009;10:1661–4. https://doi.org/10.1016/j.catcom.2009.05.004.

[103] Angelo L, Kobl K, Tejada LMM, Zimmermann Y, Parkhomenko K, Roger AC. Study of CuZn MO_x oxides (M = Al, Zr, Ce, CeZr) for the catalytic hydrogenation of CO_2 into methanol. C R Chim 2015;18:250–60. https://doi.org/10.1016/j.crci.2015.01.001.

[104] Gao P, Li F, Zhao N, Xiao F, Wei W, Zhong L, et al. Influence of modifier (Mn, La, Ce, Zr and Y) on the performance of Cu/Zn/Al catalysts via hydrotalcite-like precursors for CO_2 hydrogenation to methanol. Appl Catal A 2013;468:442–52. https://doi.org/10.1016/j.apcata.2013.09.026.

[105] Natesakhawat S, Lekse JW, Baltrus JP, Ohodnicki PR, Howard BH, Deng X, et al. Active sites and structure-activity relationships of copper-based catalysts for carbon dioxide hydrogenation to methanol. ACS Catal 2012;2:1667–76. https://doi.org/10.1021/cs300008g.

[106] Gao P, Xie R, Wang H, Zhong L, Xia L, Zhang Z, et al. Cu/Zn/Al/Zr catalysts via phase-pure hydrotalcite-like compounds for methanol synthesis from carbon dioxide. J CO2 Util 2015;11:41–8. https://doi.org/10.1016/j.jcou.2014.12.008.

[107] Li L, Mao D, Yu J, Guo X. Highly selective hydrogenation of CO_2 to methanol over CuO-ZnO-ZrO_2 catalysts prepared by a surfactant-assisted co-precipitation method. J Power Sources 2015;279:394–404. https://doi.org/10.1016/j.jpowsour.2014.12.142.

[108] Lei H, Hou Z, Xie J. Hydrogenation of CO_2 to CH_3OH over $CuO/ZnO/Al_2O_3$ catalysts prepared via a solvent-free routine. Fuel 2016;164:191–8. https://doi.org/10.1016/j.fuel.2015.09.082.

[109] Pasupulety N, Driss H, Alhamed YA, Alzahrani AA, Daous MA, Petrov L. Studies on Au/Cu-Zn-Al catalyst for methanol synthesis from CO_2. Appl Catal A 2015;504:308–18. https://doi.org/10.1016/j.apcata.2015.01.036.

[110] Dong X, Li F, Zhao N, Xiao F, Wang J, Tan Y. CO_2 hydrogenation to methanol over $Cu/ZnO/ZrO_2$ catalysts prepared by precipitation-reduction method. Appl Catal B 2016;191:8–17. https://doi.org/10.1016/j.apcatb.2016.03.014.

[111] Dong X, Li F, Zhao N, Tan Y, Wang J, Xiao F. CO_2 hydrogenation to methanol over Cu/Zn/Al/Zr catalysts prepared by liquid reduction, Cuihua Xuebao/Chinese. J Catal 2017;38:717–25. https://doi.org/10.1016/S1872-2067(17)62793-1.

[112] Guo T, Guo Q, Li S, Hu Y, Yun S, Qian Y. Effect of surface basicity over the supported Cu-ZnO catalysts on hydrogenation of CO_2 to methanol. J Catal 2022;407:312–21. https://doi.org/10.1016/j.jcat.2022.01.035.